



THE UNIVERSITY
of ADELAIDE

SCHOOL OF EARTH AND
ENVIRONMENTAL SCIENCES

NQM

A Growing Gold Miner



Geology, Geochemistry and Mineralogy of Epithermal gold ores, Moonlight Prospect, Pajingo, North Queensland.

Mineralogical-geochemical study of the prospect, with emphasis on the speciation, textures and distribution of precious metals

Matthew W. Paul¹

¹*School of Earth and Environmental Sciences, University of Adelaide, North tce, SA 5000.*

1160405

Supervisor: Nigel Cook

Co-supervisor: Cristiana Ciobanu

Contents

ABSTRACT	3
1. INTRODUCTION	4
1.1 Background	4
2. GEOLOGICAL SETTING	5
2.1 The Drummond Basin	5
3. DEPOSIT DESCRIPTION	6
3.1 Alteration	6
3.1.1 DISTAL (TO VEIN) PROPYLITIC ALTERATION	6
3.1.2 ARGILLIC ALTERATION	6
3.1.3 SILICA-PYRITE ALTERATION	6
3.1.4 EPITHERMAL QUARTZ VEINING.....	6
3.2 Moonlight Geology	7
3.3 Genetic model	7
4. SAMPLING AND ANALYTICAL METHODOLOGY	8
4.1 The sample suite	8
4.1.1 JMRD3559A	8
4.1.2 JMRD3542	8
4.1.3 JMRD3430	8
4.1.4 JMRD3253	8
4.2 Analytical methods	8
4.2.1 OPTICAL MICROSCOPY	8
4.2.2 SCANNING ELECTRON MICROSCOPE.....	8
4.2.3 ELECTRON MICROPROBE ANALYSER	9
4.2.4 LASER-ABLATION INDUCTIVELY-COUPLED PLASMA MASS-SPECTROMETRY	9
4.2.5 LA-ICP-MS MAPS	9
4.2.6 ASSAYS.....	10
4.2.7 X-RAY DIFFRACTION	10
5 RESULTS	10
5.1 Mineralogy and petrography	10
5.1.1 PYRITE TEXTURES	11
5.1.2 MINOR PHASES.....	11
5.1.3 GANGUE	12
5.1.4 GOLD MINERALS.....	12
5.2 Assays	12
5.3 Electron Micro Probe Analysis	12
5.3.1 EMPA MAP	13
5.4 Laser Ablation Inductively-Coupled Plasma Mass Spectrometry	13
5.4.2 LA-ICP-MS ELEMENT MAPS	15
5.4.3 CORRELATION TRENDS.....	16
6. DISCUSSION	17
6.1 Gold distribution	17
6.2 Silver distribution	18
6.3 Pyrite: mineral chemistry, textures and genetic implications	18
6.4 A geological model for Moonlight	19
7. CONCLUSIONS	21
8. RECOMMENDATIONS	21
9. REFERENCES	22

Geology, Geochemistry and Mineralogy of Epithermal gold ores, Moonlight Prospect, Pajingo, North Queensland

Mineralogical-geochemical study of the prospect, with emphasis on the speciation, textures and distribution of precious metals

ABSTRACT

The Moonlight deposit is a recent discovery peripheral to the Pajingo mine, located in the Drummond basin, North Queensland. The study has addressed ores and host rock in four drillcores from the upper part of the epithermal mineralization at Moonlight to determine the mineralogical and geochemical character of the mineralisation and associated alteration. Sampling was focussed on high-grade and sulfide-rich intervals. The chosen approach gave particular focus to the speciation, textures and distribution of precious metals at Pajingo and the implications of the different pyrite textures and mineral chemistry, with respect to both conditions of ore formation and the role of pyrite as a gold carrier.

Moonlight ore is largely located within altered andesites and brecciated epiclastic rocks. Veins, marked by coarse chalcedony crosscut the epiclásticos. There is evidence for a sinter above the ores, indicating formation within a sub-basin and for propylitic and argillic alteration alongside the dominant silicification.

Pyrite from both high- and low-grade sulfide-bearing intersections was analysed by laser-ablation inductively-coupled mass spectroscopy. It was found to contain an average of 69.8 ppm Au, suggesting that 'invisible gold' in pyrite contributes significantly to the overall gold balance, even if it is subordinate to visible gold. Au:Ag ratios in analysed electrum varied from 60:40 to 40:60, suggesting that there is some considerable risk of slow-floating Ag-rich electrum. Silver is present as native silver, acanthite (Ag_2S), naumannite (Ag_2Se), polybasite $[(\text{Ag,Cu})_6(\text{Sb,As})_2\text{S}_7][\text{Ag}_9\text{CuS}_4]$, pyragarite (Ag_3SbS_3) and minor hessite (Ag_2Te), as well as in solid solution and/or inclusions in pyrite.

Pyrite textures observed in the study are diverse and indicate that the epithermal system that generated the Moonlight deposit was complex and possibly multi-phase. Variation in assemblages and mineral chemistry implies substantial evolution in the physicochemical parameters of the ore-forming fluid during the life of the hydrothermal system. LA-ICPMS element mapping of a complex, zoned pyrite grain showed a core enriched in Co, Ni and Sb; onto this is superposed As, Au. Resorption and overgrowths indicate that the pyrite has been reworked. A characteristic 'dirty', feathery pyrite is of replacement origin and may have pseudomorphed chlorite that resulted from an earlier propylitic alteration.

No direct evidence was found to substantiate the working mine model in which high-grade 'bonanza' veins are predicted at depth, however observations of lithologies from the level investigated in this study are consistent with the model. The high Ag content of the Moonlight ores, together with a distinct base metal presence (sphalerite, tetrahedrite) could mean that the Moonlight system is more distal to the fluid source than Vera-Nancy and was possibly formed at somewhat cooler temperatures on the flank of the main volcanic system.

1. INTRODUCTION

The Pajingo mine, operated by Conquest Mining (formerly by North Queensland Metals (NQM)), located in the Drummond basin, North Queensland (Fig. 1a), exploits the narrow, high grade, low-sulfidation epithermal gold and silver veins of the Vera-Nancy ore body. The mine currently produces 60,000 oz/pt gold, with an average grade of 12.2 g/t (McKinstry 2009). The Moonlight prospect is a recent exploration target, located 2 km south-east of the main deposit (Fig. 1d), and has the potential to host high-grade veins, similar to those at Vera-Nancy. The lithological sequence hosting the Moonlight ores have been characterised by diamond drilling in 2008-2009.

This present study investigates the host sequence to determine the mineralogical and geochemical character of the mineralisation and associated alteration. Emphasis has been placed on the speciation, textures and distribution of precious metals at Pajingo with particular attention given to pyrite as both an indicator for the genetic conditions and as a potentially significant gold carrier. In similar deposits, lattice-bound or nanoparticulate (i.e., 'invisible') gold has been demonstrated to contribute considerably to the gold balance (Harris 1990; Vaughan & Kynin 2004). The possible implications that invisible gold has for gold recovery warrant the investigation of this problem prior to further diamond drilling. A combination of petrographic and state-of-the-art micro-analytical techniques, including quantitative trace element microanalysis and element mapping by Laser Ablation Inductively-Coupled Plasma Mass Spectrometry, were employed in order to elucidate these issues. Subsidiary goals included elucidation of an ore-forming model for the Moonlight epithermal system, establishing any differences with Vera-Nancy, and contributing to a spatial-genetic model for the deposit which could be used when considering additional drilling.

1.1 Background

In an ore deposit, gold is typically present in different forms:

- (i) Native gold and/or electrum are the dominant forms in the majority of ore deposits. Provided the gold is not too fine grained, it is generally recoverable by conventional processing techniques such as gravity separation, flotation or cyanidation.
- (ii) Invisible gold within common sulfides such as pyrite and arsenopyrite, including both lattice-bound and nanoparticulate gold. Such gold is generally only recovered if a sulfide concentrate is generated and is subject to additional processing, such as roasting or bio-oxidation.
- (iii) Gold in the form of Au-(Ag) tellurides such as calaverite, sylvanite and petzite. These minerals may not readily be recovered and telluride-bearing ores (e.g., Golden Mile, Kalgoorlie or Emperor, Fiji) may be associated with less than ideal recoveries.
- (iv) Other Au-bearing phases, such as maldonite (Au_2Bi). If present in sufficient quantities, such minerals can create processing problems.

Silver distributions may also be complex: native silver/electrum, tetrahedrite, galena and Ag-sulfosalts can all be important silver-carriers. Generally of lesser importance as Ag-hosts, but not uncommon, especially in epithermal systems, are Ag-selenides and -tellurides.

The gold and silver distribution in the Moonlight deposit was unknown before the present study. It was suspected (John McKinstry, NQM CEO, pers. comm. to Nigel Cook) that a portion of the gold may be either

present as Ag-rich electrum (less-easily floated), in the form of Au-(Ag)-tellurides, or as invisible gold hosted in pyrite.

Invisible gold may be present in pyrite and other sulfides as both nano-inclusions (Au^0) and in solid solution (Au^{+1}) (Cook & Chryssoulis 1990; Reich *et al.* 2005). The incorporation of gold into the pyrite lattice is often facilitated by the presence of arsenic, as such a lattice where each Au atom is coordinated by As atoms is more energetically favourable than configurations in which As atoms are distal or absent (Reich *et al.* 2005); indeed As is generally to be essential for the solution of gold in pyrite, though recent studies have determined that other elements (e.g. Te) may also facilitate this substitution (Cook *et al.* 2009). Au may also be present as macro inclusions or blebs within the same sulfides.

In order to achieve adequate Au recoveries from refractory ores that contain a significant portion of invisible gold, additional processing must be undertaken. The main methods include roasting, pressure oxidation, ultrafine grinding and bio-oxidation (Fraser *et al.* 1991). The application of any of these methods greatly increases the overall cost of processing, and knowing the character of the ore before developing a prospect can reduce the risk involved. Epithermal and Carlin-type deposits are the main deposit types in which invisible gold can make a significant contribution to the overall gold budget (Vaughan & Kyin 2004), such as the epithermal Emperor Gold Deposit, Fiji (Pals *et al.* 2003), and the Betze-Post Carlin-type deposit, Nevada (Leonardson & Rahn 1996).

Previous work by Baker *et al.* (2006) characterised trace element relationships in pyrite taken from 5 principal alteration zones (detailed below), from distal to proximal to high grade quartz veins of the Vera orebody, using Electron Micro Probe Analyser (EMPA) and Laser Ablation Inductively-Coupled Plasma Mass Spectrometry (LA-ICP-MS) techniques.

2. GEOLOGICAL SETTING

2.1 The Drummond Basin

The Pajingo Epithermal System (PES) is located approximately 150 km south-west of Townsville (Fig. 1a), and is hosted in the Drummond Basin (Fig. 1c), a Late Devonian to Early Carboniferous back-arc basin (Johnson & Henderson 1991). Three depositional cycles have been identified in the western subdivision (Olgers 1972; Hutton 1989). The PES, in addition to other epithermal deposits, such as the Yandan and Wirralie (Baker *et al.* 2006), occur within Cycle 1, which consists of primary volcanics and volcanoclastics, deposited in a half-graben style extensional environment (Johnson & Henderson 1991). Cycle 2 is characterised by craton-derived quartzose sandstone, conglomerates and siltstones, deposited in a fluvial environment (Olgers 1972; Henderson *et al.* 1998). Cycle 3 is composed of volcanolithic sandstones, conglomerates and intermediate to silicic volcanics (Olgers 1972; Henderson *et al.* 1998). Deposition ceased in the mid-Carboniferous, during the Kanimblan orogeny (Fenton & Jackson 1989), and the principle stage of basin inversion occurred in the mid-Triassic as a result of contractional deformation (Olgers 1972; Pinchin 1978).

Gold mineralisation is thought to be associated with major west-south-west directed extension, which resulted in north-west striking normal faults, which act as structural corridors for the movement of hydrothermal fluid. This extension is thought to be related to a back-arc basin (Johnson and Henderson, 1991). The orientations of the veins reflect the north-west strike of the regional faults (Davis, 2004).

3. DEPOSIT DESCRIPTION

The Pajingo epithermal system is the largest known epithermal system in the Drummond Basin, extending an area of over 150km² (Richards *et al.* 1998), and includes the Scott Lode, Anne, Janet, Nancy North, Cindy, Nancy, Vera, Vera South, Jandam, Zed and Sonia ore bodies (Fig. 1d). Mineralisation at the Scott Lode has been dated at 342 Ma (Perkins 1993), during the Middle Carboniferous. Gold mineralisation is distributed within epithermal quartz veins, hosted by andesitic volcanic rocks, and occurs as steeply-plunging (60-70°) ore shoots in dilatational positions within the Vera-Nancy structural corridor (Bobis *et al.* 1995; Butler *et al.* 1999). While sparse outcrops of epithermal textures assisted initial exploration of the area, the majority of the system is covered by tertiary sediments, varying in thickness from 10 to 100m. Total production, not including Scott Lode or Cindy, to May 2009, was 5.86 Mt @ 12.2 g/t Au (2.3 MOz). Moonlight forms part of the 10 km long Toby structural trend, 1.5 km south of the main Vera-Nancy system.

3.1 Alteration

Five main types of alteration have been identified at Pajingo based on observations on the Vera-Nancy system (Baker *et al.* 2006):

3.1.1 DISTAL (TO VEIN) PROPYLITIC ALTERATION

Widespread, distal propylitic alteration, dark green in colour. Primary igneous textures are commonly preserved. Mafic minerals, such as hornblende and clinopyroxene have been altered to chlorite, calcite and quartz, and plagioclase replaced by albite and calcite. Major minerals include chlorite, calcite, albite and quartz, with minor kaolinite, illite, ankerite, rutile and apatite. Pyrite is a minor component.

3.1.2 ARGILLIC ALTERATION

Occurs between propylitic and silica-pyrite zones. Cream to light brown in colour, with partial preservation of igneous textures. Mafic minerals are subject to calcite, leucoxene and chlorite alteration. Plagioclase is replaced by illite, kaolinite, ankerite and phengite. Pyrite is common, occurring as round, subhedral grains that range from 50 to 250 µm.

3.1.3 SILICA-PYRITE ALTERATION

Most proximal alteration to vein system. Light to dark grey alteration which is texturally destructive and contains quartz, illite and carbonates (mostly siderite). Idiomorphic pyrite occurs with an abundance of 2 to 5% by volume, and is coarse, typically 250 to 500 µm.

3.1.4 EPITHERMAL QUARTZ VEINING

Several styles of quartz veining present, all typical of low sulfidation epithermal deposits (Mustard *et al.* 2003). The earliest contain the highest gold grade, and is comprised of banded and moss-like textures. The banded textures are comprised of crustiform-colloform bands, formed of chalcedony, cryptocrystalline, microcrystalline and fine comb layers, each ranging from <1 mm to several cm. Pyrite occurs as fine 25 to 50 µm cubic grains.

3.1.5 LATE-STAGE CHALCEDONY

Characterised by comb, bladed carbonate replacement and amethyst, and is associated with low Au grades and rare pyrite. Late chalcedonic quartz overprints all quartz types and is typically barren and lacks sulfides.

This study did not extensively characterise the alteration assemblages, however Moonlight does appear to be comparable to Vera-Nancy, though some differences are apparent, for example, propylitic alteration at Moonlight can contain significant pyrite, with large (100-500 μm) euhedral grains common in altered andesite clasts.

3.2 Moonlight Geology

3.2.1 TERTIARY SEDIMENTS

Poorly-consolidated tertiary mudstone, siltstone (Fig. 2a), sandstone and conglomerates of the Southern Cross Formation overlie mineralisation at Moonlight, deposited in the early Eocene (Parks & Robertson 2003).

3.2.2 TERTIARY BASALT

A tertiary basalt unit (Fig. 2b) is present as two basalt stocks emplaced in the tertiary sediments, and are up to 320 m thick in drill cores. They appear discordant with bedding, and exhibit chilled margins, indicating it was intrusively placed within the sediments. The genesis and timing of this basalt is poorly understood.

3.2.3 EPICLASTICS

Epiclastic sediments of volcanic origin, composed of coarse volcanolithic sandstone that grades into laminated siltstones to mudstones (Fig. 2c), and dip 10° to the east. The unit demonstrates haematitic alteration, however areas where veining penetrates the unit, localised argillic alteration occurs (Groves, 2007).

3.2.4 VOLCANICLASTICS

The volcaniclastic layer is comprised of andesite breccias (Fig. 2g), characterised by propylitic altered sub-rounded to angular 1-15 cm andesite clasts, with a fine to coarse rock flour matrix. These breccias are interlayered with lapilli tuffs (Fig. 2f), hematite altered siltstones, and siliceous sinter layers (Fig. 2d), which represents the paleosurfaces of the hydrothermal system. This sinter layer is also inter-layered with siliciclastic sediments (Fig. 2e).

3.2.5 MOUNT JANET ANDESITE

The Mount Janet Andesite (Fig. 2h) is comprised of basaltic andesite to andesite lavas and minor lava breccias and volcaniclastic sediments. The unit is characterised by aphanitic lava flows that grade from phenocryst-poor to porphyritic lava (Groves 2007).

3.3 Genetic model

Moonlight is thought to be similar to Vera-Nancy, except subject to a lesser extent of erosion, and has been suggested to represent an intact epithermal system (citation needed). Figure 1b is a schematic model of the prospect, demonstrating the position of drillhole JMRD3559a. The current exploration model used by senior geologists for Moonlight is based on the Golden Promise Au-Ag deposit in the Republic district, Washington, USA. This model for this deposit suggests formation as part a hot spring system, with epiclastic/pyroclastic and silicified eruption breccia hosted disseminated ore near the paleosurface that are characterised by sulfide rich stringers and complex silver mineralogy and an eruption breccias that grades into a hydrothermal “vent” breccia, that contains zones of disseminated and stringer ore. Below these breccias, the bonanza-grade ore is hosted by colloform chalcedony, adularia sulfide veins (Fifarek *et al.* 1996)

.SAMPLING AND ANALYTICAL METHODOLOGY

In order to characterise the prospect, field work was undertaken in order to collect samples and log drill cores. As the prospect has yet to be developed, all lithological observations and sample material have been derived from 4 drill cores. Sixty-three samples were taken, from which 24 25 mm-diameter polished blocks were made, and examined by optical microscopy and SEM. Eleven samples were assayed, principally for Au and Ag, but also for the relationship of these elements to As, Sb and Te. Eleven samples, with a representative suite of pyrite textures, were selected for EMPA and LA-ICP-MS analysis.

4.1 The sample suite

Samples were selected from 4 diamond drill cores (Fig. 3), all from sulfide-rich areas, with particular emphasis on high grade and sulfide-rich intervals. As such, the samples were not necessarily representative of the entire deposit, but rather focussed on investigating the distribution of precious metals. The holes sampled were JMRD3559A, JMRD3542, JMRD3430 and JMRD3253. Appendix 1 contains a summary of the samples.

4.1.1 JMRD3559A

Precious metal grades throughout this drill core were consistently low, with an average grade of 0.47 g/t Au, with an exception of two silver anomalies, of over 1000 g/t over 1 m intervals. Sulfides principally occurred within chalcedonic silica veins and stringers, and with (rare) black banded silica veins; as well as minor idiomorphic pyrite in clasts of altered andesite.

4.1.2 JMRD3542

Characterised by volcanoclastic andesite, siliceous sinter and Au-rich black silica veins, Of the drill cores investigated in this project, JMRD3542 contains the greatest proportion of sulfides and an average grade of 1.3 g/t over 200 m, and as such, the largest number of samples and polished blocks are derived from this drill core.

4.1.3 JMRD3430

Composed largely of volcanoclastic sediments and brecciated, altered andesite. Gold grades are associated with black, sulfide rich quartz/carbonate veins.

4.1.4 JMRD3253

This drill core is largely bereft of sulfides; large idiomorphic grains of pyrite are only present in highly propylitic-altered andesite clasts. Gold is associated with ~40 cm wide silica veins, which are devoid of sulfides, and may represent feeder veins.

4.2 Analytical methods

4.2.1 OPTICAL MICROSCOPY

Initial analysis was undertaken using a Leitz Labourlux 12 Pol oil-immersion reflective light microscope, equipped with a digital camera.

4.2.2 SCANNING ELECTRON MICROSCOPE

SEM analysis was performed using the Philips XL30 FEGSEM with Energy Dispersive X-ray at Adelaide Microscopy Centre. The instrument was operated at beam 20eV, Spot size 4 in back-scatter electron mode.

4.2.3 ELECTRON MICROPROBE ANALYSER

EMPA analysis of pyrite and precious metal bearing phases was undertaken on the Cameca SX51 Electron Microprobe at Adelaide Microscopy Centre, using an accelerating voltage of 20kV, and a beam current of 19.5nA. Standards used were CuFeS₂ (Cu, Fe, S), CoAsS (Co, As), Au (Au), Ag₂Te (Ag, Te) Bi₂Se₃ (Bi, Se), Sb₂S₃ (Sb), HgS (Hg), Ni (Ni), CdS (Cd), MnS (Mn) and PbS (Pb).

Element maps for Ag, Au, S, Sb, Hg, Cu, Se, He and Te were prepared using the HiMax, at a resolution of 1024 x 1024 pixels, with a step size of 0.2 μm per pixel, using a 20kV, 20na beam current.

4.2.4 LASER-ABLATION INDUCTIVELY-COUPLED PLASMA MASS-SPECTROMETRY

LA-ICP-MS analysis was performed using the New Wave UP-213 Laser, coupled to an Agilent HP 7700 Quadropole ICP-MS at CODES (Centre of Excellence in Ore Deposits; University of Tasmania, Hobart). The laser was operated at frequencies of 5 or 10Hz; laser energy between 1.9 and 2.6 J/cm², with spot sizes of 25 μm for analysis and 100 μm for calibration. Each analysis ran for 90s; 30s background and 60s ablation time. The following isotopes were monitored: ⁴⁹Ti, ⁵¹V, ⁵³Cr, ⁵⁵Mn, ⁵⁷Fe, ⁵⁹Co, ⁶⁰Ni, ⁶⁵Cu, ⁶⁶Zn, ⁶⁹Ga, ⁷²Ge, ⁷⁵As, ⁷⁷Se, ⁹³Nb, ⁹⁵Mo, ¹⁰⁷Ag, ¹¹¹Cd, ¹¹⁵In, ¹¹⁸Sn, ¹²¹Sb, ¹²⁵Te, ¹⁸²W, ¹⁸⁵Re, ¹⁸⁹Os, ¹⁹⁷Au, ²⁰⁵Tl, ²⁰⁸Pb, ²⁰⁹Bi, ²³⁸U. Data reduction was undertaken according to standard methods using Fe as the internal standard. Calibration was performed using the in-house standard for sulfides (STDGL2b-2), which is composed of powdered sulfides doped with certified element solutions and fused to a lithium borate glass disk. The standard is certified for quantitative analysis of trace elements in a range of sulfide matrices (Danyushevsky *et al.* 2003 and in press). Analytical accuracy is expected to be better than 20%.

The raw analytical data for each spot analysis is plotted as a line graph and the integration times for background and sample signal selected. The counts are then corrected for instrument drift (standards were run each 1½ to 2 hours) and converted to concentration values using known values of Fe in the analyzed pyrite as an internal standard. Based on the measured concentrations, detection limits were calculated for each element in each spot analysis. These values are similar throughout the dataset since the consistent spot size has let to comparable count rates for each spot. The error on the element signal is calculated as $(\sigma/\sqrt{n}) \times 100$, where σ is the standard deviation and n the number of data points across the selected signal interval. Total analytical error (precision) is expressed as a percentage of concentration and is an expression of analytical noise. The smooth profile, and good precision, observed for almost all analyses indicates the mineral analysed to be homogeneous (Cook *et al.* 2009)

While values for Ge were reported consistently as being above detection limit, low concentrations of Ge cannot be confidently quantified, on account of interference from ⁴⁰Ar³²S and ⁴⁰Ar³²O species of the same isotopic mass (Danyushevsky *et al.* 2003). The maximum value for Ge in pyrite is 6.78 ppm, which is not significant enough to determine any geochemical trends, and as such is not further investigated in this study.

4.2.5 LA-ICP-MS MAPS

Element mapping was performed using the New Wave UP-213 Laser, coupled to an Agilent HP 4500 Quadropole ICP-MS at CODES. Trace element maps were generated by ablating sets of parallel lines in a grid across the sample. The lines were ablated at a frequency of 10 Hz, with a spot size of 10 μm, rastering at 10 μm/s. See Large *et al.* (2009) for further details of the methodology.

4.2.6 ASSAYS

Eleven assays were analysed by Genalysis Laboratory Services, using Multi-acid digest, analysed by Inductively Coupled Plasma Mass Spectrometry (A/MS), Multi-acid digest, analysed by Inductively Coupled Plasma Optical (Atomic) Emission Spectrometry (A/OES) and 25/50g Lead collection fire assay, analysed by Flame Atomic Absorption Spectrometry (FA25/AAS; FA50/AAS)

Assay data commissioned by both Newmont and NQM was also analysed. Assay data from NQM was analysed by A/OES and FA50/AAS. The methods utilised by Newmont are undocumented.

4.2.7 X-RAY DIFFRACTION

A sample of green siliciclastic material was studied by X-ray Diffraction at the South Australian Museum (SAM) in order to establish if celadonite was present.

5 RESULTS

5.1 Mineralogy and petrography

Sulfides

Pyrite	FeS ₂
Chalcopyrite	CuFeS ₂
Sphalerite	(Zn,Fe)S
Galena	PbS
Molybdenite	MoS ₂

Sulfosalts

Tetrahedrite	(Cu,Fe) ₁₂ Sb ₄ S ₁₃
Polybasite	[(Ag,Cu) ₆ (Sb,As) ₂ S ₇ [Ag ₉ CuS ₂ (S,Se) ₂]
*Sicherite	TlAg ₂ (As,Sb) ₃ S ₆

Au-Ag minerals

Electrum	AuAg
Native silver	Ag
Acanthite	Ag ₂ S
Naumannite	Ag ₂ Se
Pyrrargyrite	Ag ₃ SbS ₃
Hessite	Ag ₂ Te

Other

Hematite	Fe ₂ O ₃
Skutterudite	(Co,Ni,Fe)As ₃
Monazite	(Ce,La)PO ₄

Gangue

Apatite	Ca ₅ (PO ₄) ₃ (F,Cl,OH)
Ankerite	Ca(Fe,Mg,Mn)(CO ₃) ₂
Dolomite	CaMg(CO ₃) ₂
Calcite	CaCO ₃
Siderite	FeCO ₃
Chamosite	Fe ²⁺ ₆ Mg ₃ Al ₂ Fe ³⁺ Si ₆ Al ₂ O ₂₄ (OH) ₁₂
Sericite	KAl ₂ (AlSi ₃ O ₁₀)(F,OH) ₂
Kaolinite	Al ₂ Si ₂ O ₅ (OH) ₄
Rutile	TiO ₂
Chalcedony	SiO ₂
Adularia	KAlSi ₃ O ₈

*inferred (see text)

The major ore minerals are (arsenian) pyrite and electrum, while minor phases include chalcopyrite, sphalerite, galena, molybdenite, hematite, tetrahedrite, locally abundant acanthite-naumannite and native silver, polybasite, pyrrargyrite, skutterudite, minor hessite and a number of rare earth phases, including monazite. Figure 4 demonstrates the pyrite textures observed (see also below); Figure 5 exhibits the petrology of the minor phases and Figure 6 shows the gangue mineralogy.

Senior geologists have indicated a link between the presence of celadonite and areas of higher Au grade, however, areas indicated to contain celadonite were analysed, first with EDX, and later with X-Ray Diffraction. EDX results returned only silicon and oxygen; and the XRD spectra indicated only the presence of quartz (Appendix 2).

The majority of mineral phases were identified using EDX analysis. The stoichiometry of sulfide and Au-Ag minerals was later confirmed later EPMA (see below).

5.1.1 PYRITE TEXTURES

Pyrite at the Moonlight prospect exhibits 5 principal textures. Granular idiomorphic pyrite is present in both the alteration assemblages and the veins. The zonation patterns in these grains can be simple, complex, or absent. Figure 4a shows a representative pyrite grain in which there is an inner zone that exhibits resorption, a barren zone that contains very low concentrations of trace elements, an arsenic-rich zone, and a narrow, late, outer zone that is also devoid of trace elements. The Bladed replacement texture (Fig. 4b) appears as pseudomorphs of a bladed mineral, most likely calcite; with idiomorphic overgrowths that are richer in arsenic. This texture is present at the intersection of several blades of quartz after calcite (Fig. 7). These blades are usually 5-20 μm wide and up to 100-200 μm long. The “feathery” texture (Fig. 4c) is found only in veins, and is not associated with any idiomorphic pyrite; and indeed exhibits feathery overgrowths. The genesis of this texture remains unclear, but it may be a pseudomorph of an earlier mineral. The “Wispy” textured pyrite (Fig. 4d), together with a granular zoned pyrite, are both found in veins. The wispy replacement texture may be a relic texture of marcasite, however, in some areas, this texture resembles porphyritic plagioclase, and in others, bladed calcite. The “dirty” replacement texture (Fig. 4e) is similar to the bladed texture, except is generally much larger, usually between 20-60 μm wide and 100 μm to 1 mm long. This could still be replacement of bladed calcite, however the trace element geochemistry suggests an organic origin.

5.1.2 MINOR PHASES

Sphalerite (Fig. 5a, d) occurs as 5-30 μm -sized inclusions within pyrite, and is commonly associated with electrum and rare chalcopyrite. It is present within both veins and alteration assemblages. Skutterudite (Fig. 5b) is rare, and is present as 1-2 μm grains associated with pyrite, and is only found in veins. Hessite (Fig. 5c) is also rare, and only present in one vein in one sample, as 2-3 μm grains within pyrite. Chalcopyrite (Fig. 5d) is uncommon, and occurs with both pyrite and sphalerite, with grain sizes of 5-30 μm . Tetrahedrite (Fig. 5e) is present as 1-10 μm inclusions in or adjacent to sulfides. Acanthite and naumannite (Fig. 5f) generally occur as 1-5 μm grains in silica veins (usually one or the other), however are found together in some samples. Native silver and polybasite (Fig. 5g) occur only in two intervals from drill core 3559a, and occur together with electrum of varying composition.

Interestingly, the Moonlight prospect is almost completely devoid of tellurides; small grains of hessite only occurring as 1-5 μm -sized inclusions in pyrite in one vein, in one sample. Gold-(Ag)-tellurides are common in the upper levels of many high-grade epithermal deposits (Cook & Ciobanu 2004), and given the proposed nature of the Moonlight prospect, it is surprising to find so little in the way of telluride minerals over such a range of depths in the upper portion of the system.

5.1.3 GANGUE

Gangue minerals identified include apatite, ankerite/dolomite, calcite, chamosite, sericite, kaolinite, rutile, chalcedony and minor adularia. Chamosite and sericite occur together (Fig. 6a) as interwoven sheets, occasionally associated with kaolinite. Rutile (Fig. 6b) is commonly associated with pyrite and hematite, and is only found in the altered host rock. Ankerite and dolomite (Fig. 6c) are present as veins that exhibit compositional zonation with respect to Fe, Ca and Mg content. Late siderite stringers are present in some sections of the core, and overprint previous textures. Adularia is a very minor component at Moonlight, and is not visible in hand specimen. Microscopic adularia is, however, present around and within the porous areas of silica grains (Fig. 6d).

5.1.4 GOLD MINERALS

The major gold bearing mineral is electrum. These grains occur both free in silica veins and as microscopic inclusions in pyrite (Fig. 8). Across all samples, the Au:Ag ratio varies between 60:40 and 40:60. To determine the character of the electrum in the ore, SEM images of areas representative of the gold-rich intervals were analysed. Sixty electrum grains were measured, and reported an average grain size of 6.9 μm . Figure 9 is a histogram of grain size distribution.

5.2 Assays

Eleven samples were assayed for Au, Ag, As, Cu, Mo, Pb, Sb, Se, Te and Zn. Table 1 contains the results of these assays. The highest value for Au was found to be within chalcedonic quartz, containing 56 g/t Au. No significant trends were resolved from the data provided from these assays; the highest value of As, 756 ppm, corresponds with the second highest Au value, 4.25 ppm; however the second highest As, 714 ppm, corresponds to the second lowest Au, 0.2 ppm. It is possible that with a larger dataset, some trends may emerge.

North Queensland Metals also provided assay data for the four drill cores investigated in this study, for Au, Ag, As ($\pm\text{Sb}$, Ba), with sampling intervals of 1 m (with some exceptions). The drill cores had the following correlation coefficients for Au vs As: JMRD3542 $r=0.33$, JMRD3559a $r=0.67$, JMRD3242 $r=0.11$, JMRD3430 $r=0.36$.

5.3 Electron Micro Probe Analysis

One hundred and seventy-nine EMPA analyses of pyrite were carried out to determine the extent of chemical zoning within individual pyrite grains with respect to As, to establish the range of As-content and to identify any relationship between S and As. The grains analysed were selected on the basis of the optical and SEM work and were representative of different types of pyrite. Results are summarised in Figure 10a, a histogram demonstrating the distribution of As values. Figure 10b, in which $S(+\text{Se}+\text{Te})$ is plotted against As, demonstrates that As has an inversely proportional relationship with S. The total EMPA dataset for pyrite is tabulated in Appendix 3.

A summary of electrum analyses are shown in Table 2, and the main silver metal bearing phases are given in Table 3. A ternary phase diagram (Fig. 11) demonstrates the compositions of the various silver bearing phases with respect to their ideal compositions.

Sample MP23, from drillcore JMRD3542, contained an abundance of silver bearing minerals, such as acanthite and naumannite (as determined by SEM), however these grains were only 2-8 μm in size, and as such did not provide adequate totals when analysed by EMPA.

5.3.1 EMPA MAP

An EMPA map of a complex intergrowth of silver minerals from sample MP8; drillcore JMRD3559a, was prepared for Ag, Au, S, Sb, Hg, Cu, Se, Fe and Te (Fig. 12). Tellurium was consistently below detection limit, and as such is not shown. Due to contrast enhancement undertaken on the images, the scale between images is arbitrary; however the maps still provide information on the spatial distribution of each element. The minerals present, as determined by EMPA spots, are native silver, electrum and polybasite. Both the Ag and Au maps demonstrate variability in the Au:Ag ratio, with very diffuse boundaries between electrum and native silver, and that Hg is higher in areas of low Au:Ag. The map also indicates the presence of selenium bearing polybasite.

5.4 Laser Ablation Inductively-Coupled Plasma Mass Spectrometry

One hundred and seventy LA-ICP-MS analyses were performed. Spots were selected on the basis of their texture and chemical zonation as determined by EPMA.

LA-ICP-MS is essentially a “micro bulk” method of analysis, in which the geochemical signals of any and all minerals within the ablated volume are homogenised. The analysed volume is significantly larger than by EPMA, although the minimum detection limits are several orders of magnitude lower. The resultant spectra are subject to interpretation with respect to how elements are distributed within the minerals present; smooth profiles indicate that an element is homogeneously distributed, either in solid solution within the host or as uniformly disseminated nano-inclusions, or as large grains that are ablated for the duration of the analysis in question. The total dataset for quantitative analysis of trace elements in pyrite are given in Appendix 4.

In an effort to compare LA-ICPMS and EPMA data, descriptive statistics for As from the two methods were calculated. These are listed below (values in wt.%).

	LA-ICP-MS	EMPA
Mean	1.52	1.68
Standard Error	0.08	0.09
Median	1.32	1.37
Standard Deviation	0.98	1.30
Sample Variance	0.97	1.68
Kurtosis	0.41	0.22
Skewness	0.74	0.67
Range	5.44	7.15
Minimum	0.003	0.001
Maximum	5.44	7.15
Sum	243.09	342.11

A two-sample t-Test, assuming equal variances, returned a two-tail P value of 0.203, indicating that there is insufficient evidence to suggest that the means of the two datasets are significantly different. LA-ICP-MS and EMPA data were not necessarily taken from the same areas, or indeed the same pyrite grain. Additionally, the volume analysed by LA-ICP-MS is approximately an order of magnitude larger. Despite this, the results for both datasets were very consistent.

Pyrite grains of different textural types were targeted for comparison and contrast; in addition to distinctive textural features *within* grains, such as zonations, fractures and grain boundaries.

To comprehensively characterise pyrite geochemistry, two LA-ICP-MS maps were created for idiomorphic pyrite (Fig. 13) and “dirty” textured pyrite (Fig. 14), in addition to examination of quantitative spot analysis, including characteristic time-resolved depth profiles are directly compared (Fig. 15), a histogram of Au distribution (Fig. 16) and breakdown of correlation trends between noteworthy elements (Fig. 17).

5.4.1 LA-ICP-MS KEY FEATURES

The absolute concentration of gold varied greatly, not only within each sample, but between samples; attaining a maximum value of over 600 ppm. Pyrite of the same textural type did not always exhibit consistent geochemical trends between samples or between drill core, and as such means for Au distribution are tabulated by texture and by sample (Table 4).

Zonation of pyrite grains also plays a role in the distribution of Au and As. This is exemplified by sample MP30, in which Au and As demonstrate a predilection for the outer zonation in many grains, and are relatively sparse in the core. This is illustrated by a zoned pyrite grain (Fig. 15c, d) in which the rim (Fig. 15c) demonstrates high concentrations of Au and As (166 ppm, 19038 ppm respectively). Conversely, the core (Fig. 15d) is less enriched in these elements (5 ppm Au, 6267 ppm As). Both profiles are flat, with very minor peaks, indicating a significant portion of Au is present in solid solution.

The total dataset does not indicate a strong correlation between Au and As (Fig. 17a), however, the scatter plot visibly indicates the dependence of Au on As; given the absence of Au high, As low values, and the presence of As rich spots with negligible Au. The relationship between Au and As is eminently apparent in the element map of a zoned idiomorphic grain (Fig. 13), in which the highest values of Au and As coincide within the rim of the grain.

Interestingly, while all free Au observed in this study has been in the form of electrum, Au and Ag do not correlate in pyrite (Fig. 17f, $r = 0.51$). This is evident in the profile for a zoned pyrite grain (Fig. 15c, d). In the rim of the grain (Fig. 15c) Au and Ag are both elevated at the beginning of ablation, however after 55 seconds Ag peaks, then begins to drop sharply, while Au remains unchanged. The laser, in this case, had ablated through a Ag rich zonation, and out the other side. This apparent decoupling between the two elements, which commonly share the same distribution, is demonstrated by the element maps (Fig. 13). In much the same way that Au and As have a predisposition to occur in the rims of zoned pyrites, Ag and Sb appear to preferentially inhabit the cores of these grains.

Concentrations of Co and Ni in pyrite are worth mentioning, as while they are typically low (mean 201 ppm Co; 155 ppm Ni), values vary over 4 orders of magnitude, spiking to values of over 6,000 ppm Co and 2,800 ppm Ni within the same grain. These variations in Co and Ni do not appear to be associated with any particular texture, sample or whether the pyrite grain is within a vein or alteration. These elements are, however, generally higher in the innermost zone of zoned pyrite than in the outer. Additionally, Co and Ni concentrations are negligible in samples MP49 and MP54, the only samples in which the “wispy” and “feathery” pyrite textures are found.

In a third of the pyrite grains analysed, Mo values are over 0.5 wt.%, with a maximum of 3.1 wt.% (mean 2241 ppm) and Re, while present in very low concentrations (mean 0.3 ppm, max 1.66 ppm; only 40% of values above detection limit), demonstrates some interesting trends. Molybdenum, being a +4 cation, is largely incompatible in the pyrite lattice. Molybdenite is the only mineral that carries significant

concentrations of Re, with the exception of some rare Re-bearing phases (McCandless *et al.* 1993). Given the exceptional values of Mo, and their correlation with Re (Fig. 14e), it would be logical to conclude that at least some component of Mo is present as molybdenite inclusions, which is host to trace amounts of Re.

Thallium is above detection limit in all but one analysis; this is however a result of the low detection limit for heavier elements. Although largely present in rather low concentrations (mean 40 ppm, max 473 ppm), these concentrations are persistent and actually rather high for pyrite. The highest concentrations of Tl are found in the “dirty” pyrite textures.

Other trace elements not otherwise mentioned (V, Cr, Mn, Ga, Ge, Nb, Cd, In, Sn, W, Bi, U) were all found in low concentrations, mostly below detection limit.

Chromium, Nb, Te, W, Re, Bi and U were consistently below or slightly above detection limit. While values for Ge were reported consistently as being above detection limit, concentrations of Ge cannot be confidently quantified, on account of interference from $^{40}\text{Ar}^{32}\text{S}$ and $^{40}\text{Ar}^{32}\text{O}$ species of the same isotopic mass (Danyushevsky *et al.* 2003).

5.4.2 LA-ICP-MS ELEMENT MAPS

Two pyrite grains were mapped by LA-ICP-MS in this study element maps demonstrate the distribution of a number of elements of interest within two pyrite grains, both from drill core JMRD 2542; sample MP30. Figure 13 shows a zoned, idiomorphic grain in the alteration (Fig. 4), and Figure 14 is a “dirty” textured pyrite in the vein. The scale of these figures is in counts, and is indicative of the relative abundance of elements rather than a set concentration.

LA-ICP-MS mapping of the idiomorphic grain (Fig. 13) reveal the complex nature of the zonation pattern evident in this grain, illustrating the outer zone in which Au and As are highly enriched. This pattern is consistent with individual quantitative spot analyses from other zoned grains in this sample (Fig. 15c), in which the rim was more than 30 times more enriched in Au than the core. A minor, coincident patch of Au and As is present in the core, and in a rim between the innermost and outer zonations. Silver and Sb populate the core of zoned grains, in addition to a narrow rim at the edge of the second zonation, and largely are not associated with Au rich areas.

The innermost zonation contains Co and Ni together, as well as Cu, Ag and Sb. The second zonation is largely devoid of any significant concentration of trace elements, with the exception of a rich rim. The narrow, outermost zonation is largely devoid of any trace elements, with very minor (~100 counts) Au and As. Mercury is largely at background levels, both throughout the grain and the gangue, with the exception of the rim between zonations 2 and 3, where counts reach ~1000. Bismuth and Te (not shown) are not present in significant quantities, and do not appear to be predisposed to either the pyrite or gangue.

Aluminium, Si, K, Mn and, to an extent, Fe indicate the composition of the gangue, and that the pyrite grain is largely free of inclusions of silicates, aside from a minor rim on zonation 2. This rim could represent an inclusion of silicates and/or other phases captured by the growth of a new layer of pyrite.

The “dirty” textured pyrite (Fig. 14) does not demonstrate zoned domains to the same extent as the idiomorphic grain, however some subtle geochemical variation is present. Arsenic and Au, in contrast to do not demonstrate a predilection for any particular area of the grain, and are, for the most part, distributed evenly throughout. Note that an electrum inclusion was present in this grain, affecting the scale.

Silver and Sb occur at the highest concentrations in the centre of the “dirty” texture, however they are also present in the surrounding overgrowth in low concentrations. Copper follows a similar trend to Ag and Sb, however a Cu-rich domain is present in the bottom centre of the grain, which is depleted in most other elements, and as such may represent a chalcopyrite inclusion. Cobalt and Ni occur at the centre of what appears to be the nucleation of pyrite growth, and do not extend much further than this. Aluminium, Si, K and Mn again are only present in the surrounding gangue. The element to show the greatest difference between the two grains is Hg. While not demonstrating any particular affiliation with pyrite in the idiomorphic grain; Hg is present throughout the “dirty” textured grain, with a similar distribution to Co and Ni. Interestingly, the peak values (>10,000 counts) are associated with the electrum inclusion, which is consistent with EMPA data on electrum from other areas of the deposit.

5.4.3 CORRELATION TRENDS

The total dataset was analysed for geochemical relationships, the most significant of which are tabulated in Figure 17. Gold and As demonstrate a roughly linear relationship (Fig. 17a). The r value for the total data set for Au and As is 0.6; however, when plotting only values with >10 ppm Au, this increases to 0.75. For values <10 ppm Au, the distribution of As appears independent of Au. Interestingly, no low-As, high-Au values are present, indicating that Au is likely to be dependent on the concentration of As. Silver and Sb demonstrate a similar trend to Au and As, with a clearly visible relationship (Fig. 17b), and have a higher r value of 0.7. Gold, interestingly, correlates well with Se (Fig. 17c) when viewed as a total dataset; however when viewed per sample, no discernable trend is apparent, contrasting with Au vs As and Ag vs Sb, which in many cases, have better correlations when viewed per sample. Another noteworthy feature of the dataset, Au and Ag do not demonstrate any particular relationship (Fig. 17d) in pyrite, which is significant, as free Au is always found with Ag as electrum. While only peripheral to the more prominent features of the dataset, the relationship between Mo and Re is of interest, as Mo is the main mineral to accommodate Re (McCandless 1993); and the visible relationship coupled with an r value of 0.73 hint at the presence of micro-inclusion trace element geochemistry. Thallium and Ag (Fig. 17f) correlate very strongly; indeed demonstrating the strongest linear relationship of all plots derived from the entire dataset. Nickel and Co also correlate very well, and are a common feature of pyrite from hydrothermal ore deposits (Loftus-Hills 1967). Finally, Ag and Mo demonstrate a reasonably good correlation (Fig. 17h), the implications of which are discussed later.

6. DISCUSSION

6.1 Gold distribution

The main gold-bearing phase in the Moonlight prospect is electrum, which varies in Au:Ag ratio (Table 2), and occurs as 2-30 μm -sized grains (Fig. 9) grains, that are present both free in silica veins, and as microscopic inclusions in pyrite, also within silica veins. The latter is commonly found with sphalerite inclusions, and occasional tetrahedrite. Gold grains, either free or as small inclusions, are only found in silica veins; not in the surrounding altered host rocks.

Gold is also present in pyrite, both in solid solution, and as microscopic to submicroscopic inclusions. Figure 15 shows characteristic laser ablation profiles for pyrite, in which in one case the profile is flat indicating gold in solid solution (Fig. 15a), and, in the second case, the profile features peaks indicating the presence of mineral inclusions (Fig. 15b). Inferences about the chemical state of Au in pyrite can also be made by plotting Au against As (Fig. 18) and comparing the results with the experimentally determined solubility limit of Au in pyrite (Reich *et al.* 2005). In the case of Moonlight, most data points plot below, if not well below, the solubility line (i.e. solid solution), but there are, nevertheless, some values plotting above the line where the gold is likely to be present as Au^0 .

One overarching feature of Au distribution in pyrite is that the texture does not necessarily have complete agency over the concentration of Au, and indeed the absolute amount of Au in pyrite varies spatially as well as texturally. All textures observed demonstrate the facility to host significant Au, up to 100's of ppm. However, in all samples in which pyrite occurred within both a silica vein, and within altered host rock, the mean Au values of the vein-hosted pyrite were always in excess of those hosted by alteration assemblages.

Assay data, both from NQM and those requisitioned as part of this project, failed to establish any significant relationship between Au and As in the bulk ore. Given the nature of whole rock analysis, this is, however, unsurprising. Since Au is present as free grains, often within the same veins as auriferous arsenian pyrite, Au values may fluctuate greatly with respect to As; additionally, Au-free arsenian pyrite grains are also present, typically within low grade intersections, which nevertheless contribute considerable As to the overall rock geochemistry.

The results of previous work by Baker *et al.* (2006) on pyrite from 4 geological settings at Pajingo are vastly different to those at Moonlight. The most remarkable disparity is the concentration of Au in pyrite; while Au was present in almost every bulk analysis, and often in significant concentrations, little to no Au (max 2.54 ppm) was present in the pyrite samples analysed by Baker *et al.* Furthermore, that study was unable to make any cogent association between Au and As, and surmised that invisible Au was present in any significant capacity. These factors could be explained by the sampling strategy, pyrite found in vein-distal assemblages at Moonlight were characteristically low in Au, although often with significant and highly varying As content. Additionally, the pyrite analysis given by Baker *et al.* (2006) do not address the geochemical variation inherent with *textural* variation. At Moonlight, textures within pyrite grains exhibit a vast contrast in trace elements endowments (Fig. 13), and although Baker *et al.* identified zonation with respect to As using EMPA, these zones were not necessarily targeted for comparison of Au values.

6.2 Silver distribution

As with Au, the majority of silver is present as electrum. Minor silver-bearing phases include acanthite, naumannite, polybasite, pyragarite and native silver. Many of these minerals are present in complex, multiphase intergrowths (e.g., Fig. 12); some such intergrowths are visible in hand sample. Although quantitative data cannot be given due to the bias towards sulfide-rich intervals in this study, such Ag-minerals may play an important role in governing the distribution of silver in the deposit. A considerable portion of the silver is also contained in pyrite, both in solid solution, and as micro-inclusions of native silver or silver-bearing minerals, and as electrum.

6.3 Pyrite: mineral chemistry, textures and genetic implications

While many elements may be present in solid solution in pyrite, there is evidence that micro to nano-inclusions contribute to the geochemical distribution of some trace elements. Molybdenum, for example, is an element which is not readily incorporated into the pyrite lattice (Huston *et al.* 1995), and as such, the extremely high values as those reported here are likely to represent inclusions - in this case, probably molybdenite. This is also suggested by the Re concentrations which correlate well with Mo, as molybdenite is one of the few minerals which is able to incorporate Re into its crystal lattice.

The correlations between Ag, Sb, Tl and Mo in pyrite can be indicative of a number of possible scenarios. It is possible that all four are in solid solution in pyrite (though this is probably unlikely for Mo), as these elements generally demonstrate smooth LA-ICPMS depth profiles. Other possibilities include Mo being present as inclusions, and that Ag is in solid solution with pyrite, stabilised by Sb in the absence of As; or that Ag, Sb and Tl are present together as inclusions of a Tl-bearing mineral such as sicherite, $\text{TlAg}_2(\text{As,Sb})_3\text{S}_6$.

The wide range of unusual pyrite textures observed at Moonlight can assist with development of a genetic model for the Moonlight epithermal system. Firstly, the style of texture that is most indicative of the evolution of the epithermal system is zoned, idiomorphic pyrite (Fig. 4a). Compositional imaging preserved within these grains (Fig. 13) provides information about the conditions during their formation. The first generation of pyrite is enriched in Co, Ni, Ag, Sb and Cu, indicating that the early ore-forming fluids carried these elements. A stage of resorption, evident by the ragged nature of the inner zones, indicates that a second pulse of fluid interacted with the earlier pyrite, causing their partial destruction. This was followed by further deposition. The second growth phase within the zoned pyrite grains is largely barren, but the outermost rim is high in Ag and Sb, and shows a clearly idiomorphic shape, meaning no further resorption occurred. The outermost zones indicate a dramatic change in fluid chemistry with Au and As strongly enriched.

The bladed pyrite texture (Fig. 4b) occurs only in sections of the core that exhibit quartz pseudomorphs after bladed calcite, and indeed occur at the intersection of 'blades' of quartz (Fig. 7). The 'bladed' component of these pyrite grains is bespeckled and dirty, with clean, idiomorphic overgrowths. This suggests that the inner portions of pyrite formed concurrently with quartz, directly replacing calcite, followed by a later stage of pyrite growth.

The 'feathery' pyrite (Fig. 4c) is clearly pseudomorphic after another mineral, possibly chlorite, as mentioned above, possibly indicating that mineralization took place after propylitic alteration. Previous work by Groves (2007) identified chlorite in veins near the intersection this sample was derived from, lending credence to this theory. Geochemically, pyrite with this texture demonstrates some unusual

trends, most notably of which is the lack of Co or Ni, which are consistently below detection limit, contrasting with most other pyrite textures, which contain these elements in at least modest concentrations. 'Wispy' textured pyrite (Fig. 4d) appears texturally different to the "feathery" pyrite, occurring as elongate 'wisps' that are typically clean. This texture is also interpreted as a pseudomorph of an earlier mineral, possibly calcite; geochemically, however the 'wispy' texture is more similar to the 'feathery' pyrite, rather than the 'blady' texture, particularly with respect to Ag, Mo and Tl.

The 'dirty' textured pyrite (Fig. 4e) is only found in drill core JMRD3542; however it is widespread throughout Au-rich intersections in the silicified volcanoclastic andesite. Several characteristics; notably the morphology, mineralogical associations and unusual trace element geochemistry; hint at the origin of this texture. The elongate, lath-like appearance of the inner, dirty portion of these grains is reminiscent of molybdenite when viewed parallel to the cleavage plane, and is found in samples in which molybdenite is present. The texture possibly demonstrates a progressive replacement from molybdenite to 'dirty' textured pyrite (Fig. 19). Finally, and perhaps most compellingly, pyrite of this textural type contains anomalously high concentrations of Mo, in some cases in excess of 3 wt.% (Appendix 4), while immediately adjacent 'clean' pyrite grains contain little.

Inferences about the order in which these textures formed can be drawn from their geochemical signature. Pyrite that has undergone multiple stages of growth (Fig. 13) is more likely to be among the first to have formed, and which has subsequently been subjected to later fluid pulses. The high levels of Co and Ni in the cores of these older grains suggests that early fluids were enriched in these elements. The Au- and As-rich outer zones indicate that the later fluids supplied Au to the system. Textural varieties of pyrite that are characteristically low in Co and Ni, and enriched in Au and As, namely the 'feathery' and 'wispy' textures, are interpreted to have formed late in the evolution of the ore-forming system at Moonlight.

6.4 A geological model for Moonlight

The Moonlight system is interpreted by senior exploration geologists as an intact epithermal system, with target high-grade quartz feeder veins hosted by andesite located at depth, covered by volcanic breccias and capped by a sinter layer, approximating the (eroded) paleosurface, which sits under epiclastic material. This volcanic suite lies under a Tertiary cover sequence. The basis for this model has been described by Fifarek *et al.* (1996) for the Golden Promise deposit, Republic district, Washington, USA.

The majority of the Tertiary sediments and Tertiary basalt are not preserved in the drill cores at Moonlight, as these sections of the stratigraphy were drilled by RC methods rather than diamond drilling. The sections that are preserved do not exhibit any hydrothermal veining or alteration, and indeed, post-date the mineralisation by ~300 Ma. These lithologies overlie epiclastic sediments, which are characteristically hematite-altered. Quartz veining sporadically penetrates the epiclastics. The sinter and siliciclastics designate the interface between the sediments and underlying volcanoclastics. Several sinter layers, interlayered with siliciclastic sediments, are present between 428 and 433 m in drillhole JMRD3542. Siliceous sinter deposits as such, are, however, not intersected in all drill cores. Silicified andesite volcanoclastic breccias underlie the sinter, and are characterised by widespread black silica/pyrite veining, high Au grades and extensive propylitic alteration. Fifteen metres below the sinter, quartz pseudomorphs after blady calcite are evident in silica veins. Bladed calcite is widely accepted as evidence of boiling (e.g. Simmons & Christenson 1994, Etoh *et al.* 2002).

The sinter layer commonly approximates the paleosurface of the epithermal system, analogous to contemporary hot springs, such as in Rotoura, New Zealand (Hedenquist & Henley 1985); however, this does not necessarily represent paleosurface at the time of mineralisation. Phreatic eruptions near the end of the formation may have blown the top off the system, or there was considerable erosion prior to deposition of the cover sequences. The unconformable contact between the Tertiary sediments and the epiclastic sequence, and the fact that the sinter is not present in all drill cores, suggest that the sinter indeed may not represent the paleosurface at the time of mineralisation.

Alteration styles at Moonlight follow the 'Golden Promise' model in that there are zones of strong argillic to propylitic alteration that were later overprinted by silica alteration. This is most evident in volcanoclastic breccias that host to argillic and/or propylitic altered clasts, which have, in turn, been subject to silicification as part of the silica infill. The Moonlight and Golden Promise systems are also structurally similar, Golden Promise forming on the Eureka fault as part of the Republic graben, and Moonlight forming on a half-graben as part of the Toby fault-splay structure. Other similarities include the poorly-mineralised nature of the epiclastic unit, and the presence of fine-grained electrum, black auriferous sulfide-rich stringers and several complex silver phases, including acanthite, naumannite, pyragarite, polybasite and tetrahedrite in the volcanoclastics.

Key differences between the prospect and the 'Golden Promise' model are that pyroclastics were not observed at Moonlight, and suggest the character of eruptions were more phreatic, as opposed to phreatomagmatic at Golden Promise. Additionally, at Golden Promise, there is no mention of the presence of boiling textures above the large mineralised veins that comprise the ore. Even though quartz pseudomorphs after bladed calcite are taken as indicative of boiling at Moonlight, boiling might not have been single-stage, and may not have been the only mechanism of Au deposition. Other discrepancies include the fact that some mineral phases known from Golden Promise were not found at Moonlight (stephanite, aguilarite, miargyrite, uytenbogaardtite and jalpaite); it is possible, however, that these minerals are present, but would only be seen in a larger-scale mineralogical study.

Ultimately, from direct observation and literature review, the stratigraphy, mineralogy, structural features and alteration assemblages of the sequences investigated in this study are largely consistent with the upper levels of the Golden Promise deposit (Fifarek *et al.* 1996). As such, this continues to suggest that Moonlight has potential to host similar high-grade veins at depth. Recent drilling of the Moonlight prospect has intersected a 3.7 m quartz vein (NQM Quarterly Report, 22 October 2010). Although assay results on these holes did not return any significant Au, this does not discount the possibility of high-grade veins as depth. The mineralisation in the Vera-Nancy orebody is also largely 'hit and miss' with respect to whether quartz veins are mineralised or not. The presence of a non-mineralised quartz vein still confirms the presence of previously undiscovered wide 'Vera-Nancy-style' veins, and may yet host significant ore. Further work is required to understand the controls on mineralised vs. barren veins.

7. CONCLUSIONS

Invisible gold in pyrite contributes significantly to the overall gold balance in the Moonlight orebody, although this is subordinate to visible gold. The present data, with its focus on sulfide-rich intervals does not, however, allow a quantitative assessment.

- The pyrite investigated in this study, taken from both high- and low-grade sulfide-bearing sections, has an average of 69.8 ppm Au.

Precious metals are distributed through a number of phases throughout the Moonlight prospect

- Silver is present as native silver, acanthite, nau mannite, polybasite, pyragarite and minor hessite, as well as in solid solution and/or inclusions in pyrite.
- Au:Ag ratios in electrum from the studied samples varied from 60:40 to 40:60, suggesting that there is some considerable risk of slow-floating Ag-rich electrum.
- Telluride minerals play a negligible role in the distributions of precious metals.

Pyrite textures observed in the study are diverse and indicate that the epithermal system that generated the Moonlight deposit was complex and possibly multiphase, with substantial evolution in the physicochemical parameters of the ore-forming fluid during the life of the hydrothermal system.

The lithologies at the level investigated by this project were largely consistent with the postulated model. The likely presence of high-grade feeder veins at depth was, however, not confirmed by the new information.

8. RECOMMENDATIONS

To further understand that nature of the “dirty” pyrite, HR-TEM analysis would provide insight into whether the elements found in high concentrations in pyrite of this texture are present in solid solution, or as mineral inclusions; and if so, what minerals.

In terms of exploration, deeper, targeted drilling to confirm or deny the presence of high grade veins., using parent holes to guide daughter holes, in order to reduce the costs, around the recently intersected wide quartz veins

Acknowledgements

First and foremost I wish to thank Nigel Cook and Cristiana Ciobanu, for their tireless efforts in the preparation and execution of this project. Angus Netting, Benjamin Wade, Ken Neubauer and John Terlet of Adelaide Microscopy are gratefully thanked, and without whom much of the analysis undertaken in this project would not have been possible. Leonid Danyshevsky, Sarah Gilbert and Ian Little of the University of Tasmania are thanked for their assistance with the LA-ICP-MS work, Inna Lykova for her XRD analysis of chalcedony. Brentan Grant and Peter Browne and all the staff from North Queensland Metals are thanked for their assistance and geological insight. CODES staff will be co-authors in eventual publication of the LA-ICP-MS data and element maps. The South Australian Museum is acknowledged for access to microscope facilities. Lastly, NQM are gratefully acknowledged for the funding that made this project possible.

9. REFERENCES

- BAKER T., MUSTARD R., BROWN V., PEARSON N., STANLEY C. R., RADFORD N. W., & BUTLER I. 2006. Textural and chemical zonation of pyrite at Pajingo: a potential vector to epithermal gold veins. *Geochemistry: Exploration, Environment, Analysis*, **6**, 283-293.
- BOBIS R. E., JAIRETH S. & MORRISON G. W. 1995. The anatomy of a Carboniferous epithermal ore shoot at Pajingo, Queensland: setting, zoning, alteration, and fluid conditions. *Economic Geology*, **90**, 1776–1798.
- BUTLER I., MURPHY T. & PARKS J. 1999. Vera South: Discovery History. *Exploration Under Cover'99*, *aig.asn.au*.
- COOK N. J. & CHRYSOULIS S. L. 1990. Concentrations of “invisible gold” in the common sulphides. *Canadian Mineralogist*, **28**, 1-16.
- COOK N. J. & CIOBANU C. L. 2004. Bismuth tellurides and sulphosalts from the Larga hydrothermal system, Metaliferi Mts., Romania: paragenesis and genetic significance. *Mineralogical Magazine*. **68**, 301–321.
- COOK N. J., CIOBANU C. L., MAO J. 2009. Textural control on gold distribution in As-free pyrite from the Dongping, Huangtuliang and Hougou gold deposits, North China Craton (Hebei Province, China). *Chemical Geology*, **264**, 101-121
- DANYUSHEVSKY L. V., ROBINSON P., MCGOLDRICK P., LARGE R. R., GILBERT S. 2003. LA-ICPMS of sulphides: evaluation of an XRF glass disc standard for analysis of different sulphide matrixes. *Geochimica et Cosmochimica Acta*, **67**, 23.
- DAVIS B. K. 2004. Pajingo: A Structural Context: *Unpublished Newmont report*.
- DAVIS B. K., & HENDERSON R. A. 1996. Rift-phase extensional fabrics of the back-arc Drummond Basin, eastern Australia. *Basin Research*, **8**, 371-381.
- ETOH J., IZAWA E., & WATANABE K.. 2002. Bladed quartz and its relationship to gold mineralization in the Hishikari low-sulfidation epithermal gold deposit, Japan. *Economic Geology*, **97**, 1841-1851.
- FENTON M. W. & JACKSON K. S. 1989. The Drummond Basin: low-cost exploration in a high-risk area. *Australian Petroleum Exploration Association Journal*, **29**, 220-234.
- FIFAREK R. H., DELVIN B. D. & TSCHAUDER R. J. JR. 1996. Au-Ag mineralization at the Golden Promise Deposit, Republic District, Washington: Relation to graben development and hot spring processes. *Geology and Ore Deposits of the American Cordillera Proceedings*, **2**, 1063-1088.
- FRASER K. S., WALTON R. H. & WELLS, J. A. 1991. Processing of refractory gold ores. *Minerals Engineering*, **4**, 7-11, 1029-1041.
- GROVES S. R. 2007. The Geology and Genesis of the Moonlight Prospect, Pajingo Epithermal System, Northeast Queensland: an investigation of a high-level, low sulfidation epithermal sysem. *MSc thesis, University of Tasmania (unpublished)*.

- HARRIS D. C. 1990. The Mineralogy of gold and its relevance to gold recoveries. *Mineralium deposita*, **25**, S3-S7.
- HEDENQUIST J. W. 1991. Boiling and dilution in the shallow portion of the Waiotapu geothermal system, New Zealand, *Geochimica et Cosmochimica Acta*, **55**, 10, 2753-2765
- HEDENQUIST J. W. & HENLEY R. W. 1985. Hydrothermal eruptions in the Waiotapu geothermal system, New Zealand; their origin, associated breccias, and relation to precious metal mineralization. *Economic Geology*, **80**, 1640-1668.
- HENDERSON R. A., DAVIS B. K. & FANNING C. M. 1998. Stratigraphy, age relationships and tectonic setting of rift-phase infill in the Drummond Basin, central Queensland. *Australian Journal of Earth Sciences*, **45**, 579-595.
- HUSTON D. L., SOEY S. H., SUTER. G. F., COOKE D. R. BOTH R. A. 1995. Trace Elements in Sulfide Minerals from Eastern Australian Volcanic-Hosted Massive Sulfide Deposits: Part I. Proton Microprobe of Pyrite, Chalcopyrite, and Sphalerite, and Part II. Selenium Levels in Pyrite: Comparison with $\delta^{34}\text{S}$ Values and Implications for the Source of Sulfur in Volcanogenic Hydrothermal Systems. *Economic Geology*, **90**, 1167-1196.
- HUTTON L. J. 1989. A stratigraphy and tectonic model for the Drummond Basin and its relationship to gold mineralisation. *North Queensland Gold 1989 Conference. AUSIMM, Townsville*, 31-40.
- JOHNSON S. E., & HENDERSON R. A., 1991. Tectonic development of the Drummond Basin, eastern Australia: backarc extension and inversion in a Late Palaeozoic active margin setting. *Basin Research*, **3**, 197-213.
- LARGE R. R., DANYUSHEVSKY L., HOLLIT C., MASLENNIKOV V., MEFFRE S., GILBERT S., BULL S., SCOTT R., EMSBO P., THOMAS H., SINGH B. & FOSTER J. 2009. Gold and Trace Element Zonation in Pyrite Using a Laser Imaging Technique: Implications for the Timing of Gold in Orogenic and Carlin-Style Sediment-Hosted Deposits. *Economic Geology*. **104**, 635-668.
- LEONARDSON R. W., & RAHN J. E. 1996. Geology of the Betze-Post gold deposits, Eureka county, Nevada. *Geology and Ore Deposits of the American Cordillera: Symposium Proceedings, Reno/Sparks, Nevada, April 1995*, 61–94.
- Loftus-Hills, G. 1967. Cobalt, nickel and selenium in sulphides as indicators of ore genesis. *Mineralium deposita*, **2**, 228-242.
- MCCANDLESS T. E., RUIZ J. & CAMPBELL A. R. 1993. Rhenium behavior in molybdenite in hypogene and near-surface environments: Implications for Re-Os geochronometry. *Geochimica et Cosmochimica Acta*, **57** (4),889-905.
- McKINSTRY J. 2009. CEO's Report to the 2009 AGM, North Queensland Metals. *Unpublished report*.
- MUSTARD R., BAKER T., BROWN V. & BOLT S. 2003. Alteration, paragenesis and vein textures, Vera-Nancy, Australia. *EGRU Contribution*, **61**, 99–10
- OLGERS F. 1972. Geology of the Drummond Basin, Queensland. *Bureau of Mineral Resources, Geology and Geophysics. Australia Bulletin*, **132**, 78.
- PALS D.W., SPRY P.G. & CHRYSOULIS S. 2003. Invisible Gold and Tellurium in Arsenic-Rich Pyrite from the Emperor Gold Deposit, Fiji: Implications for Gold Distribution and Deposition. *Economic geology*, **98**, 479-494.

- PARKS J., & ROBERTSON I. D. M. 2003. Pajingo Epithermal Gold Deposits, NE Queensland. *C.R.M., Regolith Expression of Australian Ore Systems: CRC LEME Monograph.1-4.*
- PERKINS C. 1993. Isotopic Dating of Precious and Base Metal Deposits and their Host Rocks in Eastern Australia. *Final Report April 1993, AMIRA Project, 334.*
- PINCHIN J. 1978. A seismic investigation of the eastern margin of the Galilee Basin, Queensland. *BMR, Journal of Australian Geology and Geophysics, 3*, 193-202.
- REICH M., KESLER S. E., UTSUNOMIYA S., PALENI, C. S., CHRYSOULIS S. L. & EWING R. C., 2005. Solubility of gold in arsenian pyrite. *Geochimica et Cosmochimica Acta, 69*, 2781-2796.
- RICHARDS D. R., ELLIOT G. J. & JONES B. H. 1998. Vera North and Nancy gold deposits, Pajingo. *Geology of Australia and Papua New Guinea Mineral Deposits. The Australasian Institute of Mining and Metallurgy, Melbourne.* 685-690
- SIMMONS S. S., & CHRISTENSON B. W. 1994. Origins of calcite in a boiling geothermal system. *American Journal of Science. 294.* 361-400.
- VAUGHAN J. P. & KYIN A. 2004. Refractory gold ores in Archaean greenstones, Western Australia: mineralogy, gold paragenesis, metallurgical characterization and classification. *Mineralogical magazine, 68*, 255-277.

Figures

Figure 1: Location map, schematic diagram and regional geology.	26
Figure 2: Moonlight lithologies.	27
Figure 3: Schematic logs of drill cores.	28
Figure 4: Pyrite textures	29
Figure 5: Minor ore phases	30
Figure 6: Gangue mineralogy	31
Figure 7: Quartz pseudomorph after blady calcite	32
Figure 8: Reflected light photo -micrographs of electrum	33
Figure 9: Histogram of gold grain distribution	34
Figure 10: Summary figures for EMPA data on arsenic in pyrite	35
Figure 11: Ternary phase digram of silver bearing phases	35
Figure 12: EMPA map of silver mineral intergrowths	36
Figure 13: LA-ICP-MS map of idiomorphic pyrite grain	37
Figure 14: LA-ICP-MS map of 'dirty' pyrite grain	38
Figure 15: Time-resolved LA-ICPOMS depth profiles	39
Figure 16: Histogram of gold distribution in pyrite from LA -ICP-MS data	40
Figure 17: Binary plots of element conce ntrations from LA-ICP-MS data	41
Figure 18: Gold vs Arsenic binary plot against solubility limit	42
Figure 19: Descriptive figure for pyrite replacement	43

Tables

Table 1: Assay data	44
Table 2: EMPA data for electrum	45
Table 3: Summary of EMPA data on silver minerals.	46
Table 4: Summary of LA -ICP-MS data	47

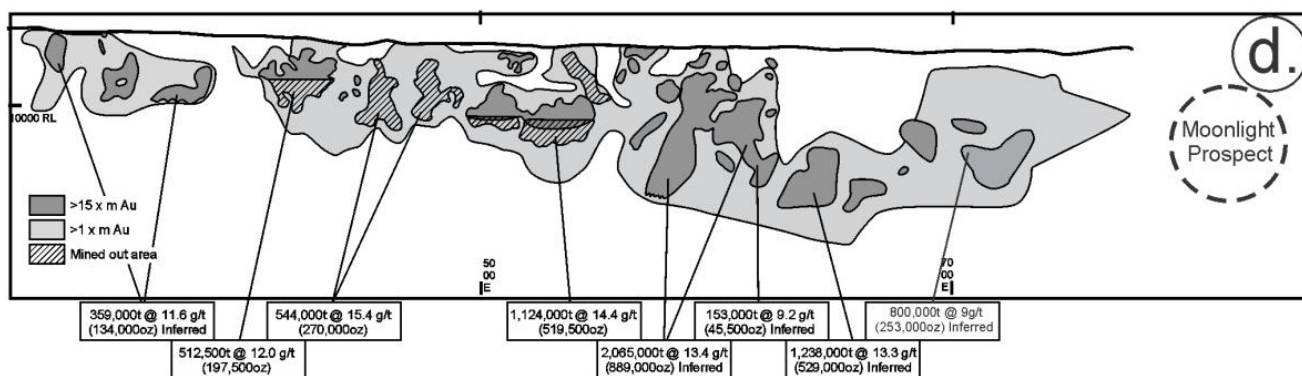
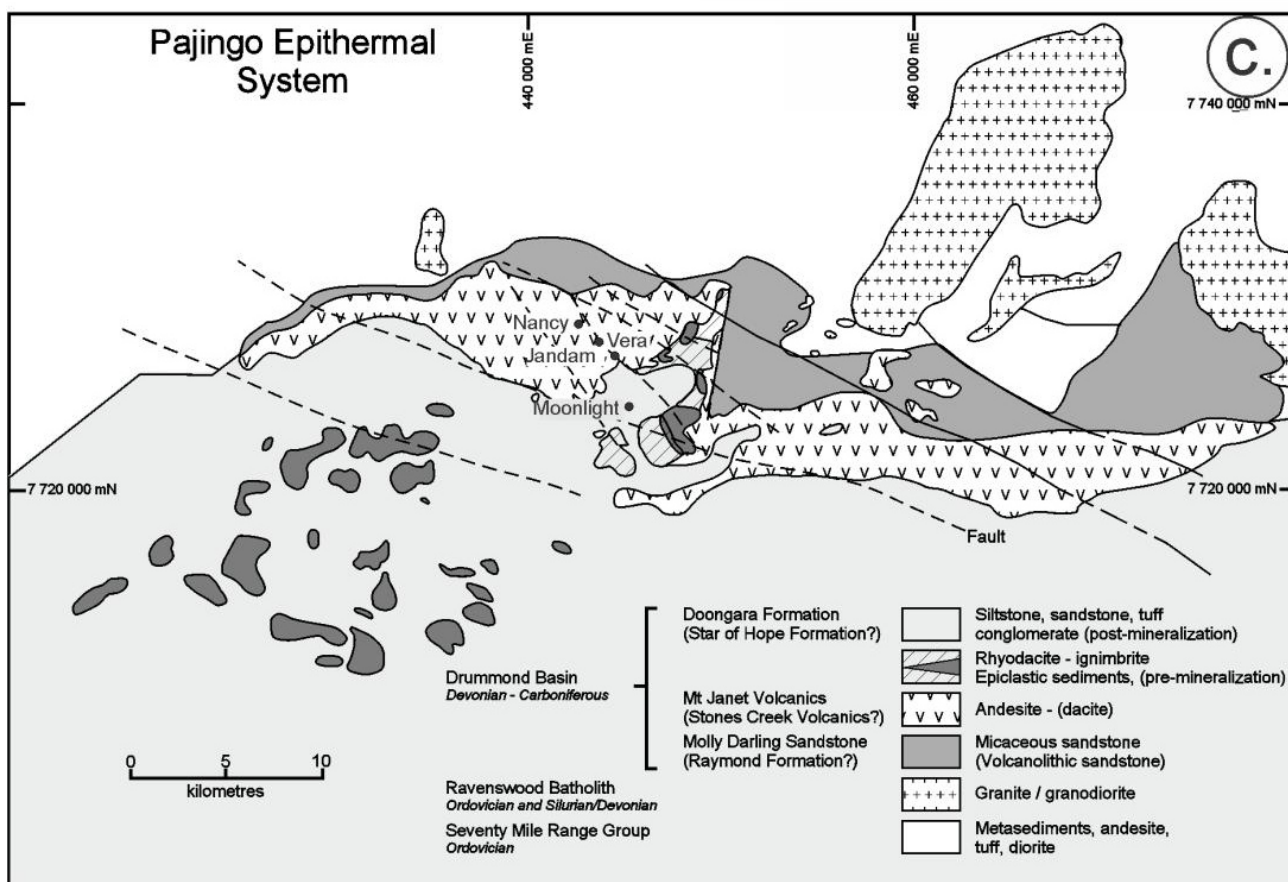
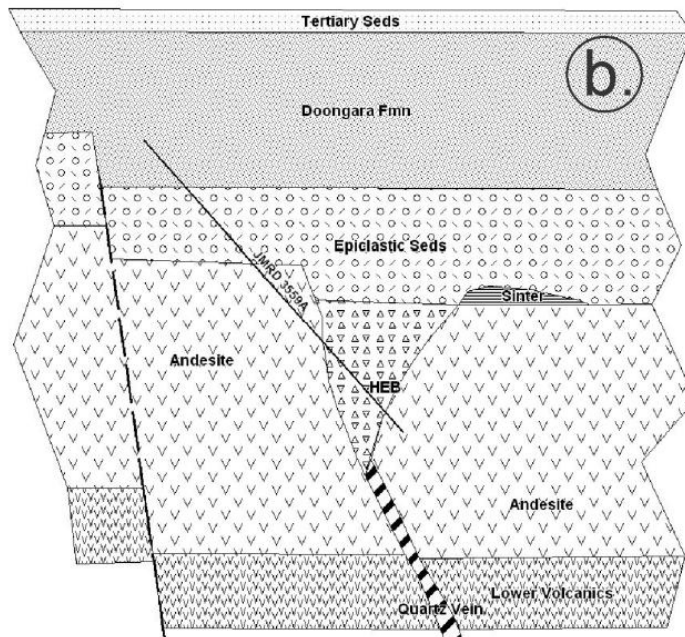
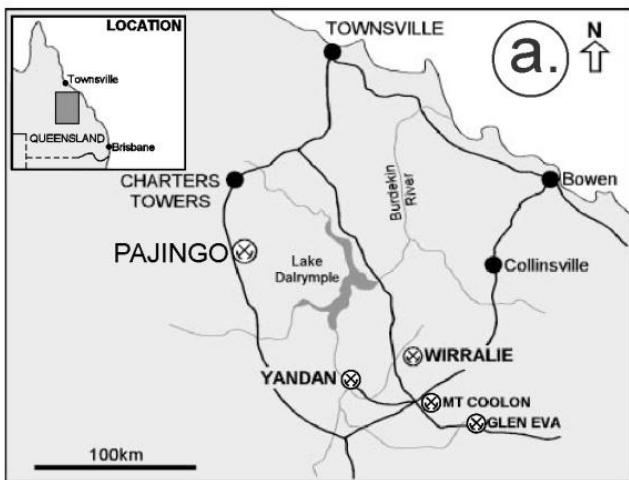


Figure 1: a) Location map of the Pajingo epithermal system with respect to Townsville, and other mines in the Drummond basin; b) schematic section of the Moonlight prospect; c) map of the regional geology of Pajingo; d) a cross section demonstrating the ore bodies exploited at the Pajingo mine, with respect to the Moonlight prospect (adapted from Baker *et al.* 2006).

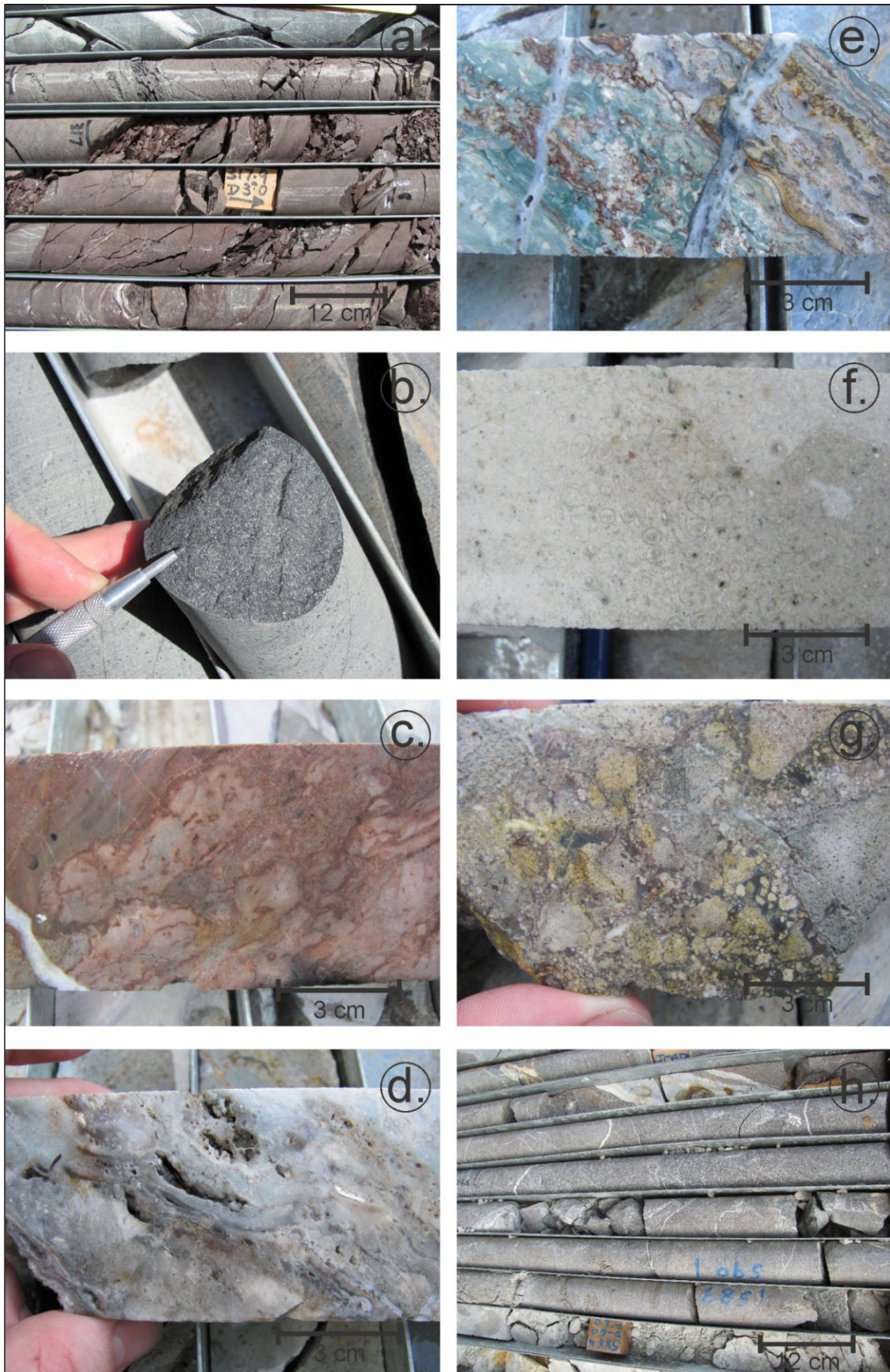


Figure 2: Photographs of characteristic lithologies at Moonlight. a) Mudstones of the tertiary sediments; b) tertiary basalt; c) haematitic epiclastic sediments; d) silicified sinter; e) sicliclastic sediments in sinter layer; f) lapilli tuff in volcaniclastic andesite layer; g) volcaniclastic andesite fragmental; h) (mostly) unaltered andesite with minor quartz veining.

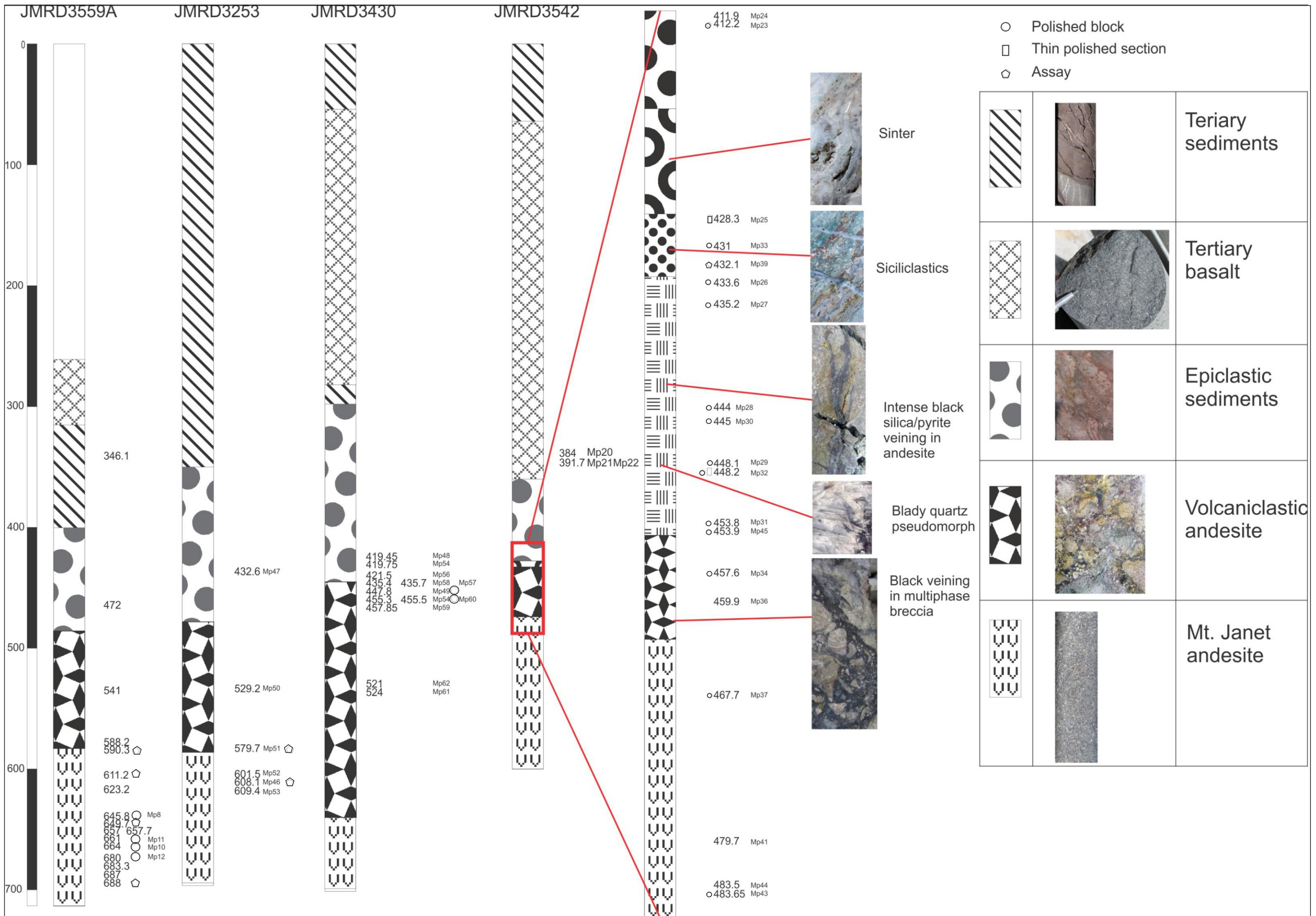


Figure 3: Schematic log of drill cores logged in this study, demonstrating the key lithologies and sampling intervals. Scale is in metres.

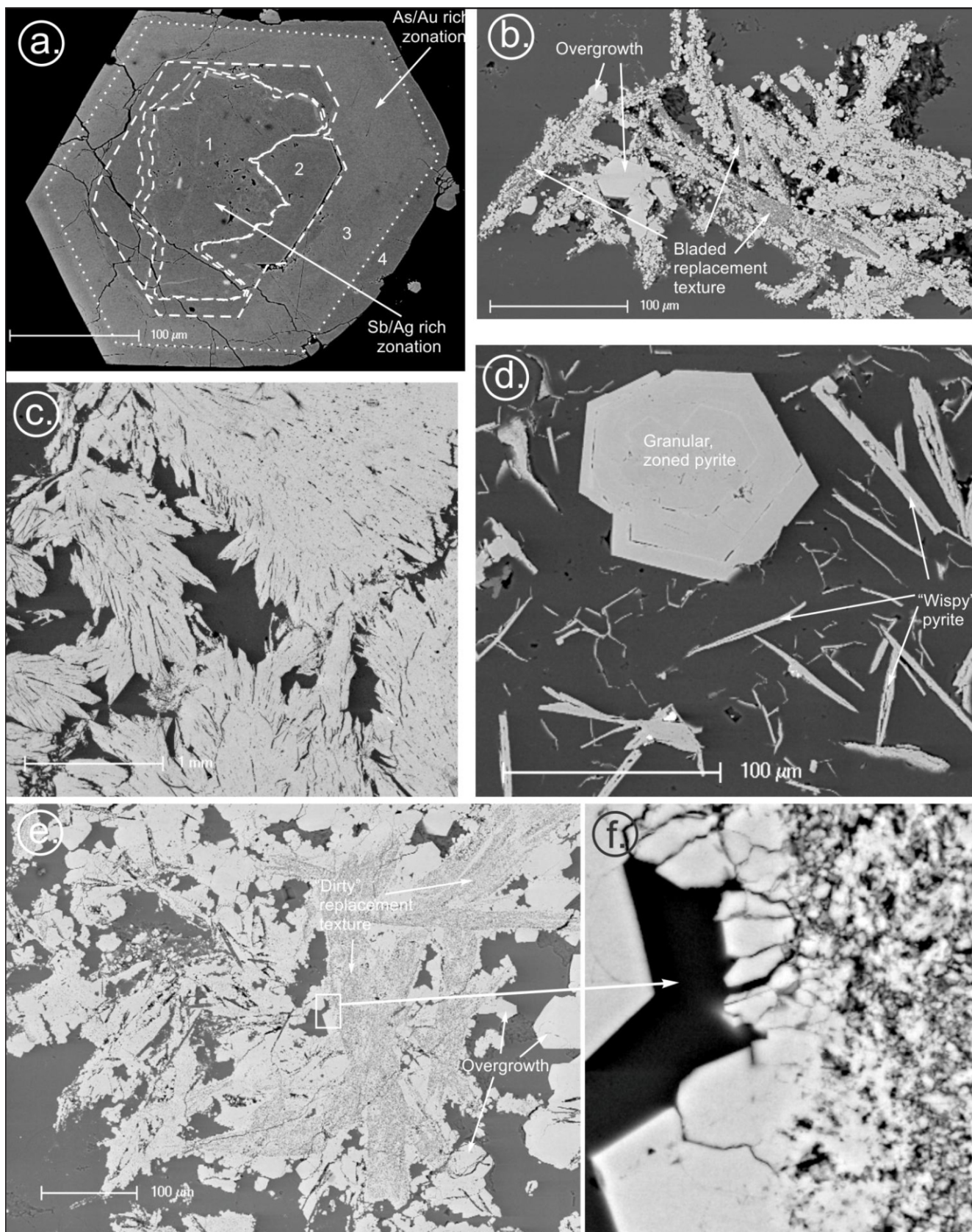


Figure 4: Back-scatter electron images of the different textures in pyrite at Moonlight. a) Zoned idiomorphic pyrite grain, with 4 compositionally distinct zones; b) Pyrite with a bladed replacement texture with idiomorphic overgrowths; c) "Feathery" pyrite with a felty, matted texture; d) "Wispy" lamellar pyrite and a zoned, idiomorphic pyrite grain; e) Coarse "dirty" pyrite replacement texture with idiomorphic overgrowths; f) enlargement of overgrowths on "dirty" textured pyrite.

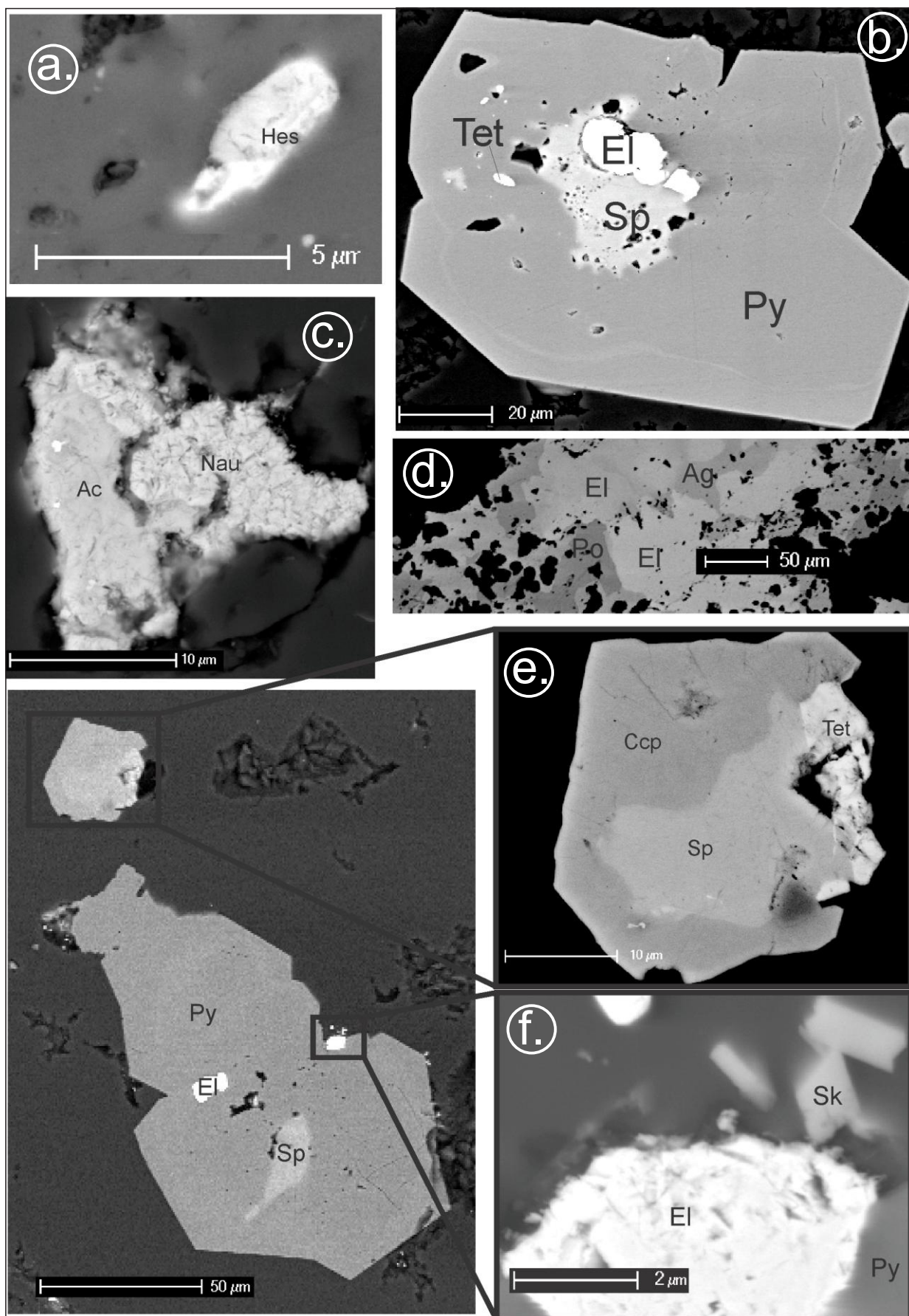


Figure 5: Back-scatter electron images of minor phases. a) Small hessite grain inclusion in pyrite, in silica vein; b) Sphalerite, electrum and small tetrahedrite inclusion in pyrite, in vuggy silica vein, cutting hematite altered andesite; c) A grain containing both acanthite and naumannite in silica vein; d) Native silver and electrum of varying composition and polybasite; e) inset of chalcopyrite replacing sphalerite, with associated tetrahedrite; f) inset of skutterudite grains adjacent to an electrum inclusion in pyrite. Abbreviations: Ac=Acanthite, Ag=Native silver, Ccp=Chalcopyrite, El=Electrum, Hes=Hessite, Nau=Naumannite, Po=Polybasite, Py=Pyrite, Sk=Skutterudite, Sp=Sphalerite, Tet=Tetrahedrite .

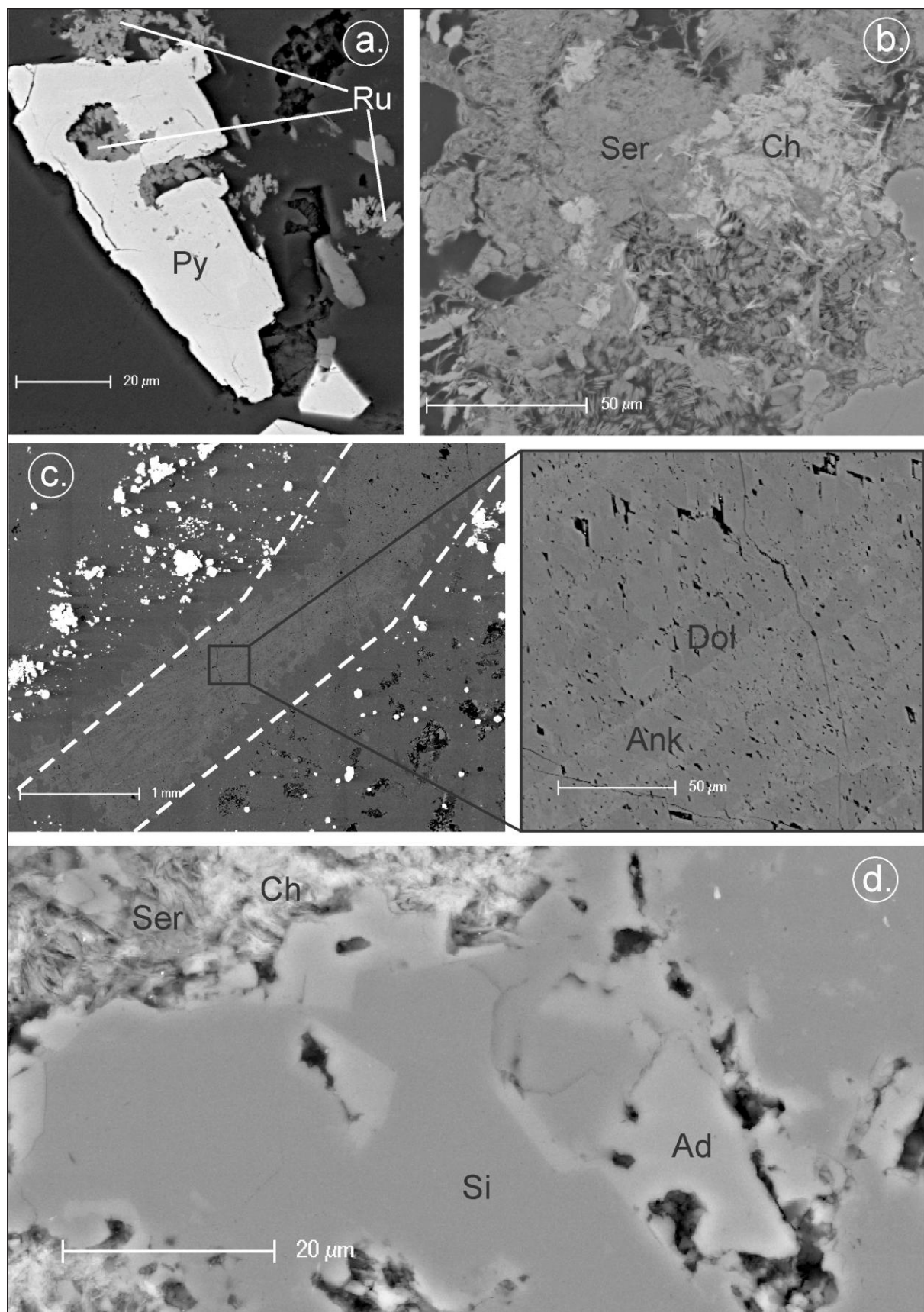


Figure 6: Back-scatter electron images of gangue assemblages a) Rutile grains in silica and pyrite; b) Sericite and chamosite intergrowths; c) Carbonate vein separating silica/pyrite vein from alteration assemblages, enlargement inset of dolomite/ankerite intergrowths; d) Microscopic adularia replacing silica rims and through pores. (Ad=Adularia, Ank=Ankerite, Ch=Chamosite, Dol=Dolomite, Py=Pyrite, Ser=Sericite, Si=Silica, Ru=Rutile)

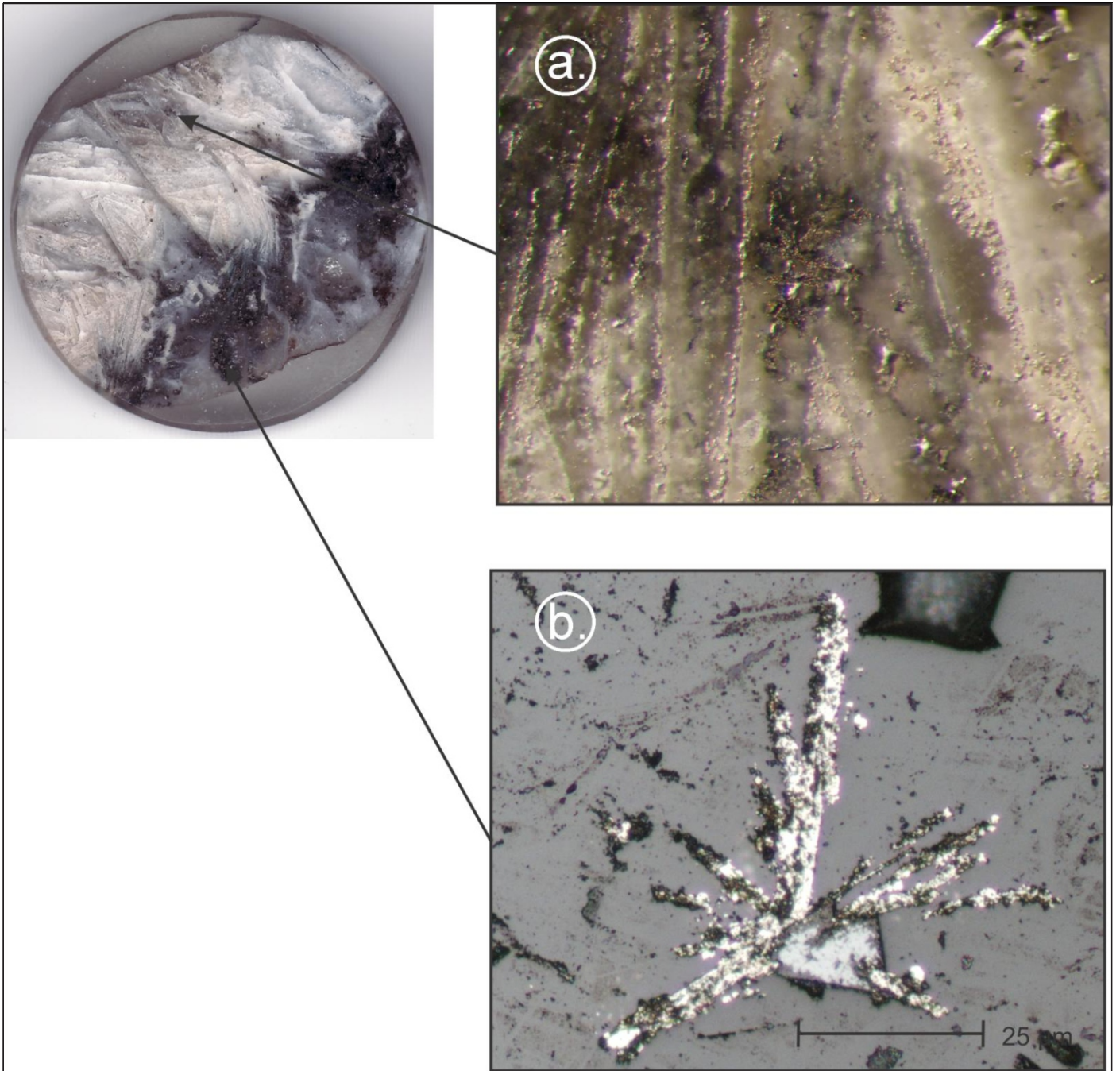


Figure 7: Sample MP32, demonstrating blady quartz pseudomorph after calcite, with a) dissecting microscope image at 400x magnification, and b) reflective light photo micrograph. Pyrite demonstrates a blady texture, similar to that of the quartz.

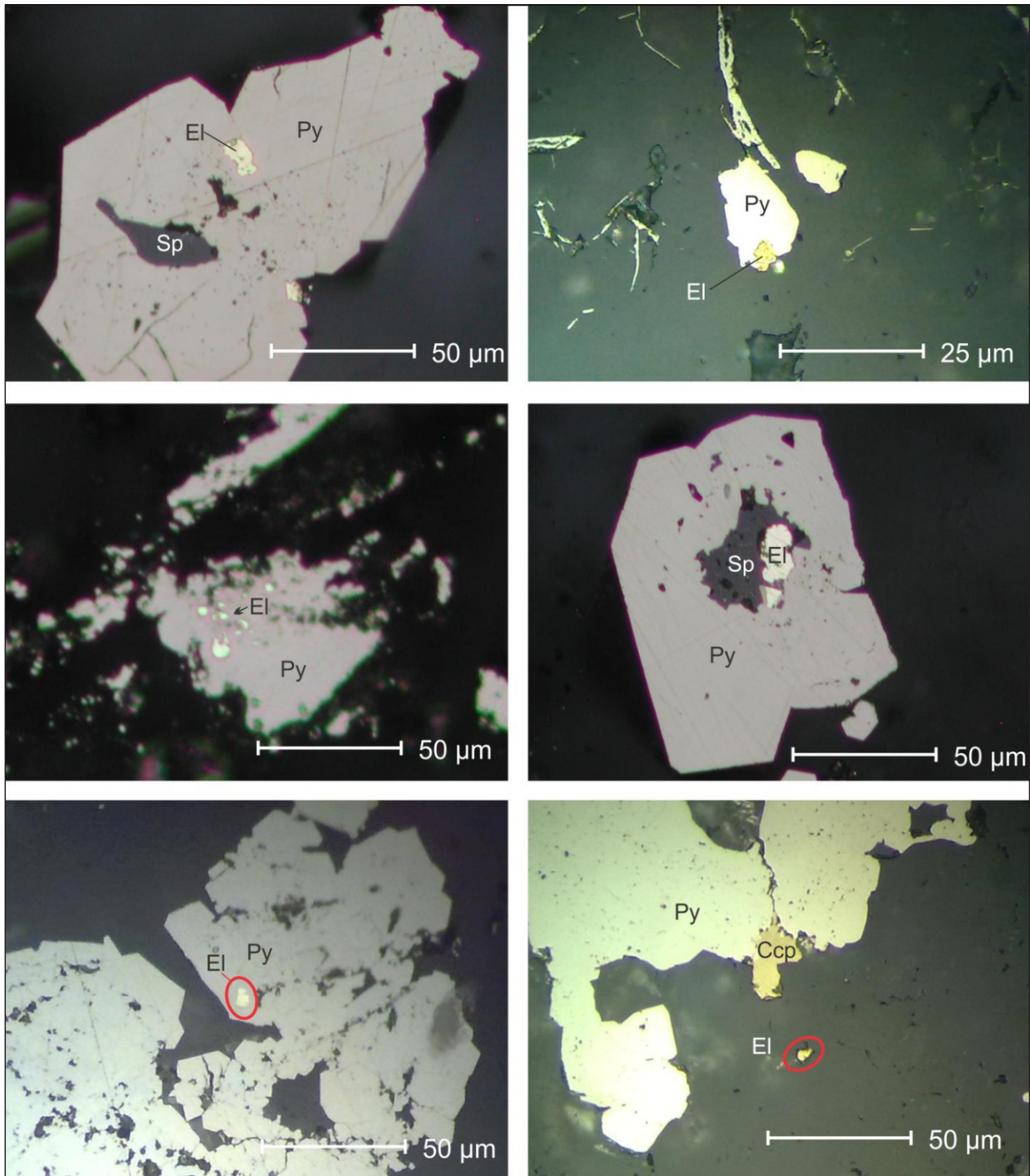


Figure 8: Reflected light photo micrographs of electrum. a) two electrum inclusions in pyrite with sphalerite; b) electrum bleb at the boundary of a pyrite grain; c) a collection of 1-5 μ m electrum inclusions in a pyrite grain; d) electrum and sphalerite inclusion in the core of a pyrite grain; e) electrum near grain boundaries of a pyrite aggregate; f) electrum free in silica adjacent to a pyrite/chalcopyrite grain. (Ccp=Chalcopyrite; El=electrum; Py=pyrite; Sp=sphalerite)

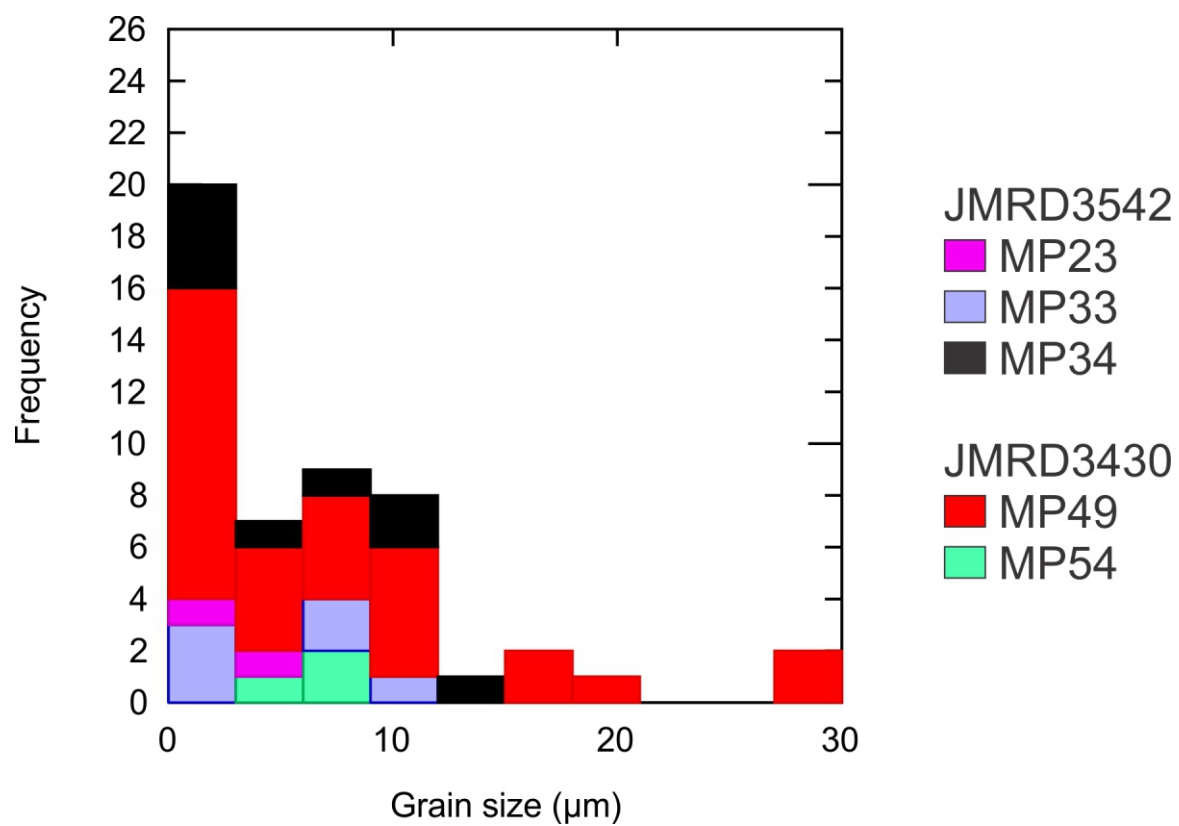


Figure 9: Histogram of gold (electrum) grain size distribution

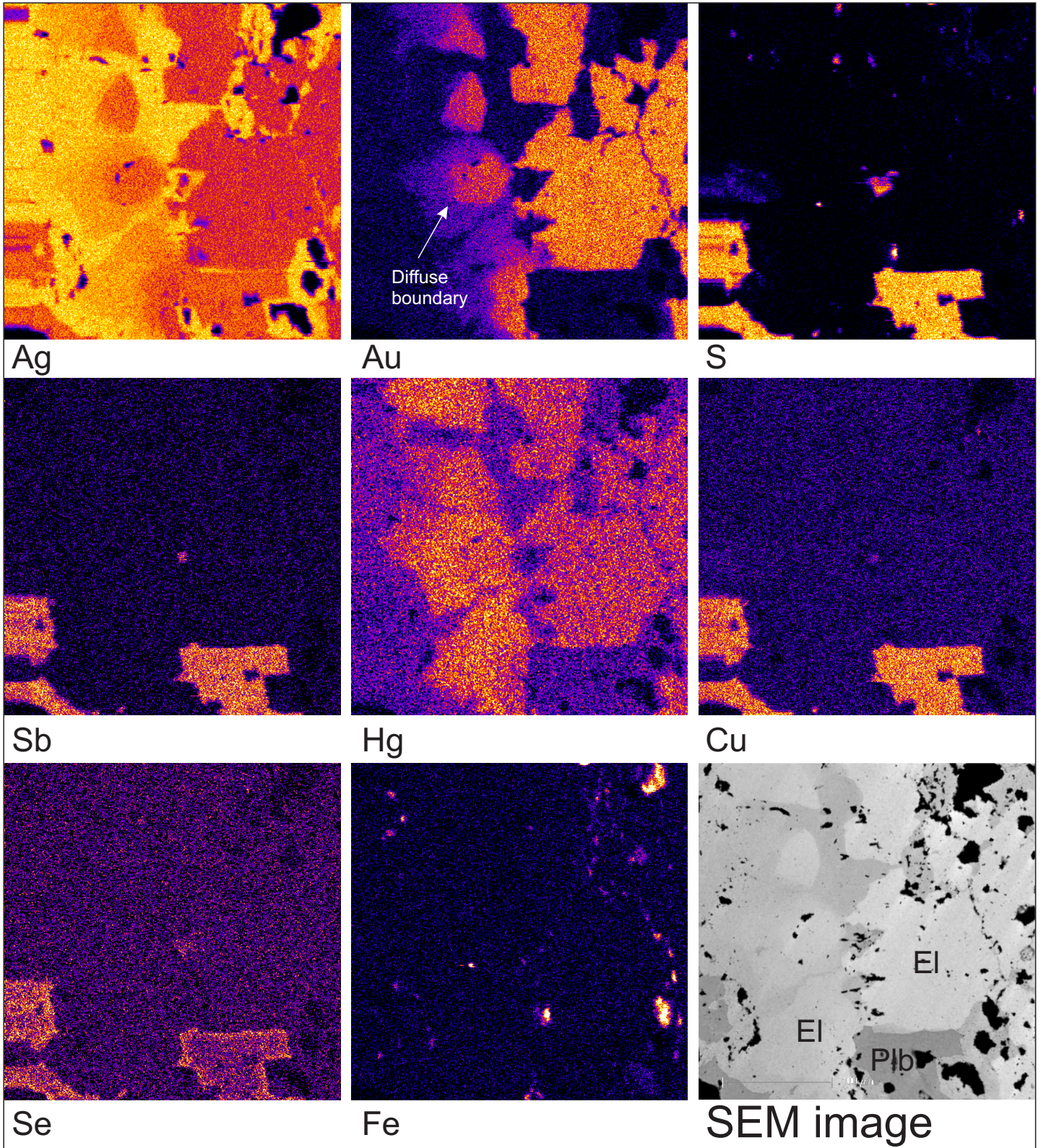


Figure 12: X-ray element maps of a complex intergrowth of silver minerals for a range of Ag, Au, S, Sb, Hg, Cu, Se and Fe. Colour shades indicate the relative abundance of each element at each spot (pixel). The colour scale is, however, arbitrary and not necessarily directly comparable between elements. Back-scatter electron image of the mapped area bottom right. (Ag= native silver; EI=electrum; Plb=Polybasite)

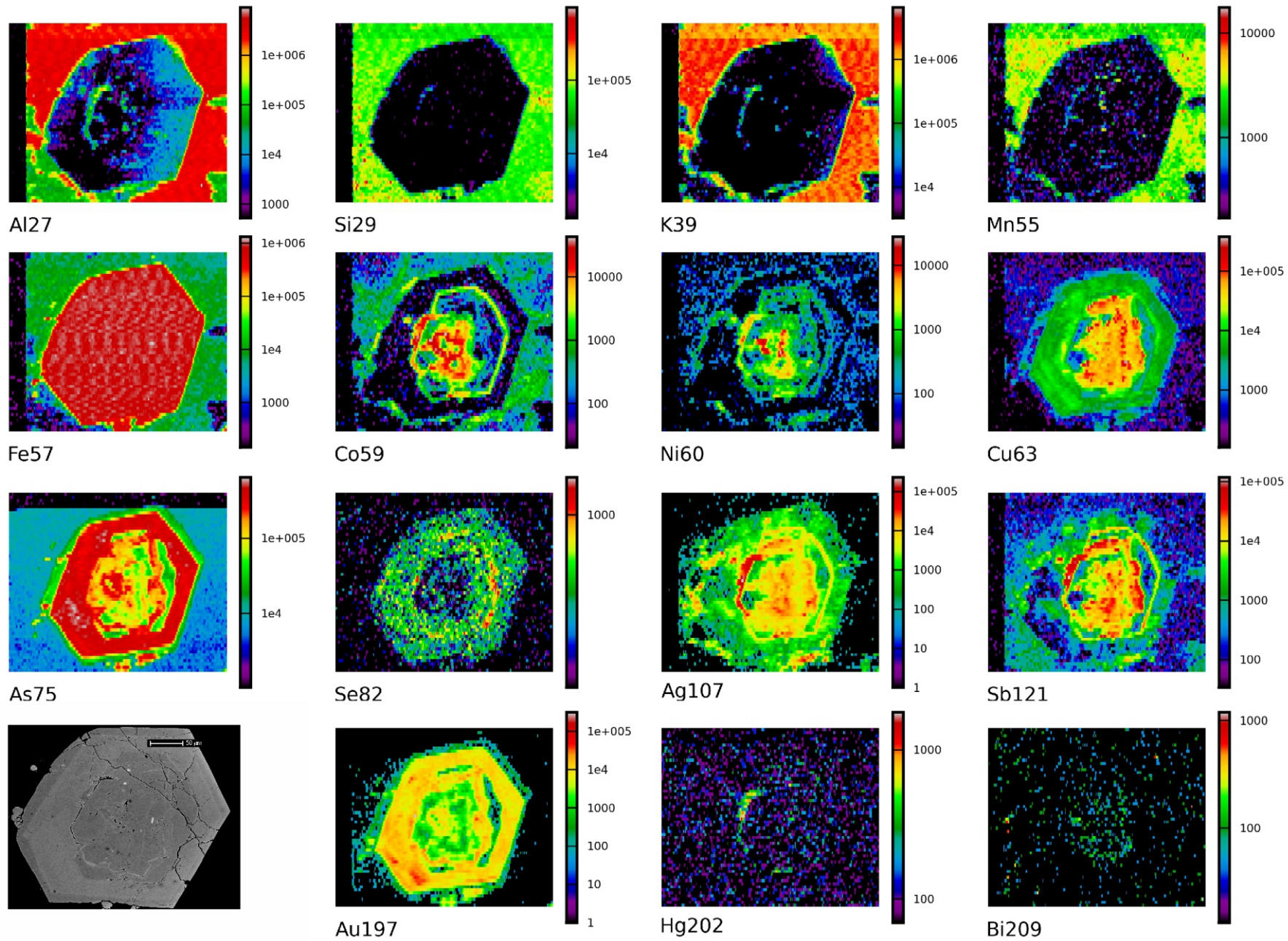


Figure 13: LA-ICP-MS element maps for Al, Si, K, Mn, Fe, Co, Ni, Cu, As, Se, Ag, Sb, Au, Hg and Bi in an idiomorphic arsenian pyrite grain (sample MP30, sample type). Colour shades indicate abundances of each element (number of counts). Back-scatter electron image of grain bottom left. Colour scale is in number of counts; scale bar on BSE image is 50 µm.

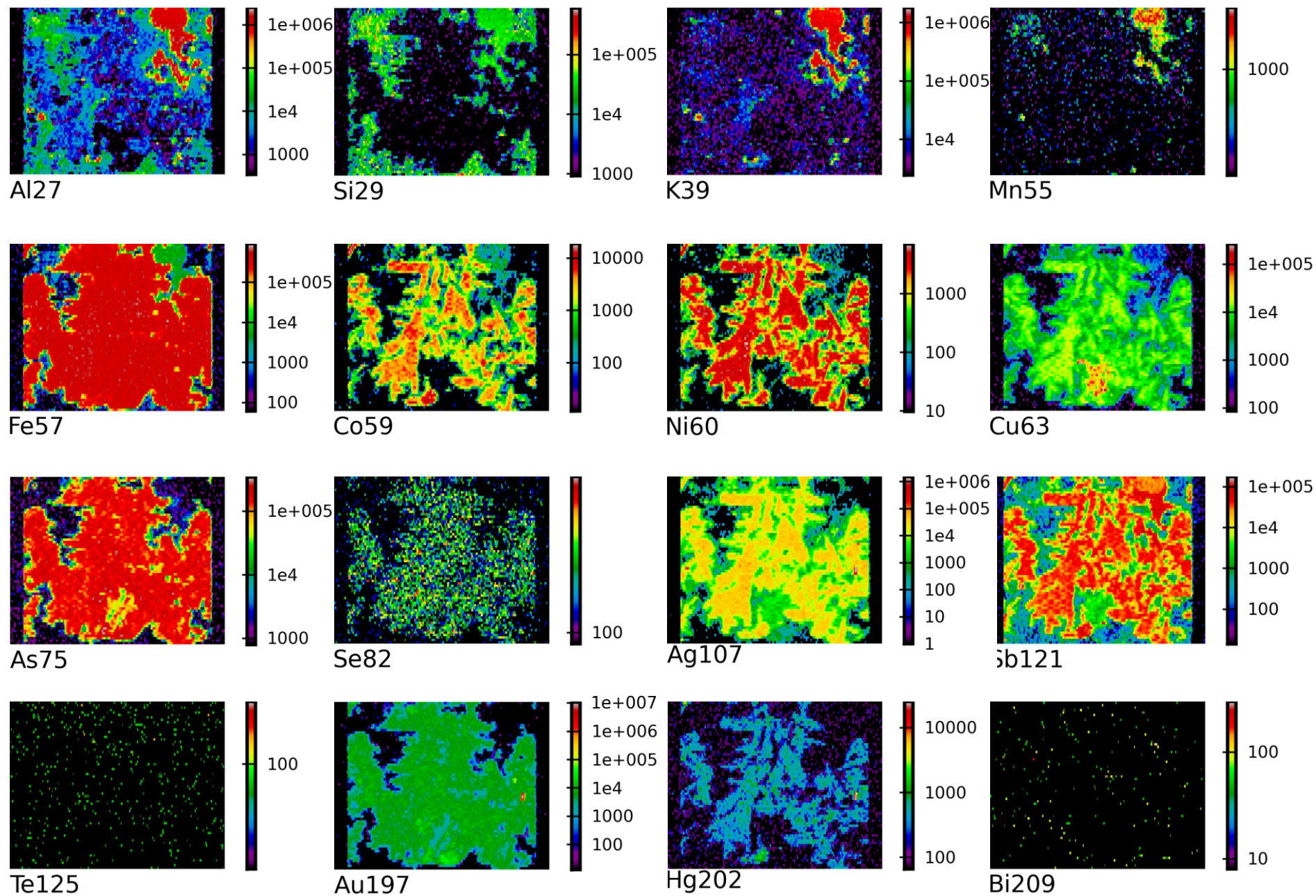


Figure 14: LA-ICP-MS element maps for Al, Si, K, Mn, Fe, Co, Ni, Cu, As, Se, Ag, Sb, Te, Au, Hg and Bi in a "dirty" textured arsenian pyrite grain (sample MP30). Colour shades indicate abundances of each element (number of counts).

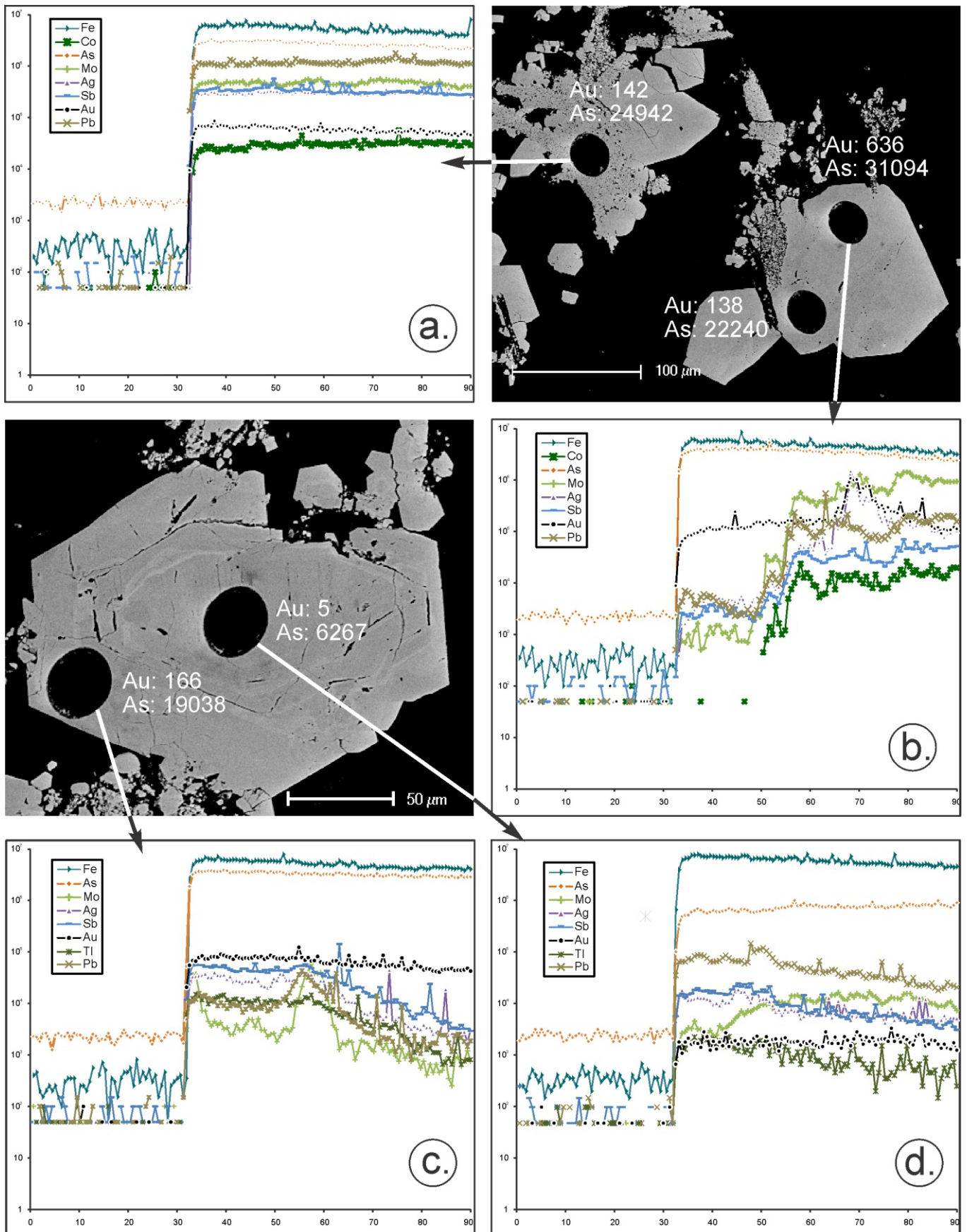


Figure 15 Four representative LA-ICP-MS time-resolved depth profiles in pyrite from sample MP30. LA-ICP-MS holes are seen as black circles on the back-scatter electron images. All elements displayed in a) show smooth spectra, indicating that these elements are likely to be in solid solution. This contrasts with (b), in which sudden spikes indicates the presence of mineral inclusions. Profiles c) and d) represent the rim and core of a zoned pyrite grain. Note the marked difference in the Au and As concentrations measured in the two spots (numbers on the BSE image are in ppm), and the corresponding depth profiles.

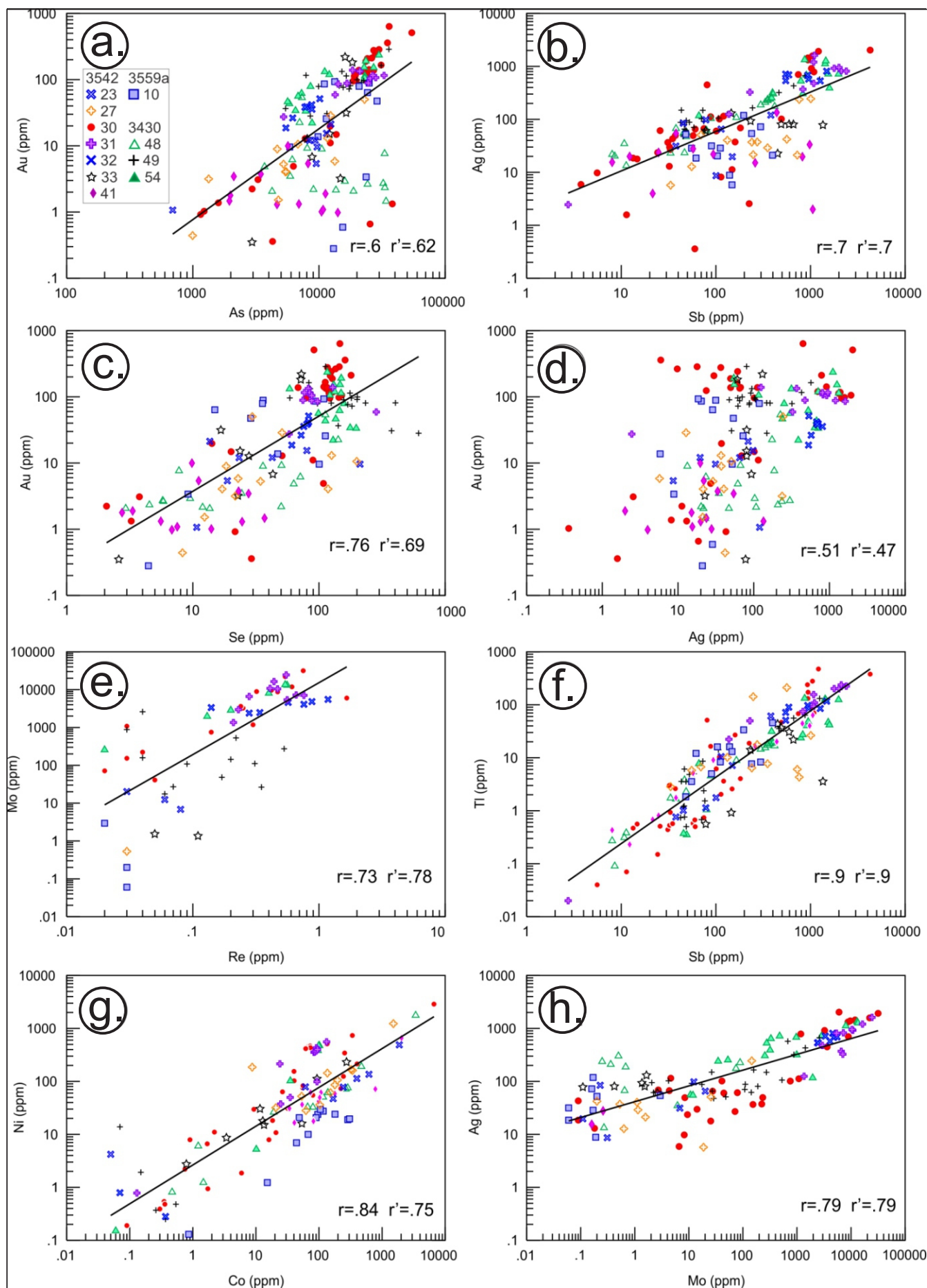


Figure 17: Binary plots of element concentrations in pyrite from LA-ICP-MS spots (complete dataset), r =Pearson's correlation coefficient, r' =Spearman's rank correlation coefficient. a) Au vs. As; b) Ag vs. Sb; c) Au vs. Se; d) Au vs. Ag; e) Mo vs. Re; f) Tl vs. Sb; g) Ni vs. Co; h) Ag vs. Mo.

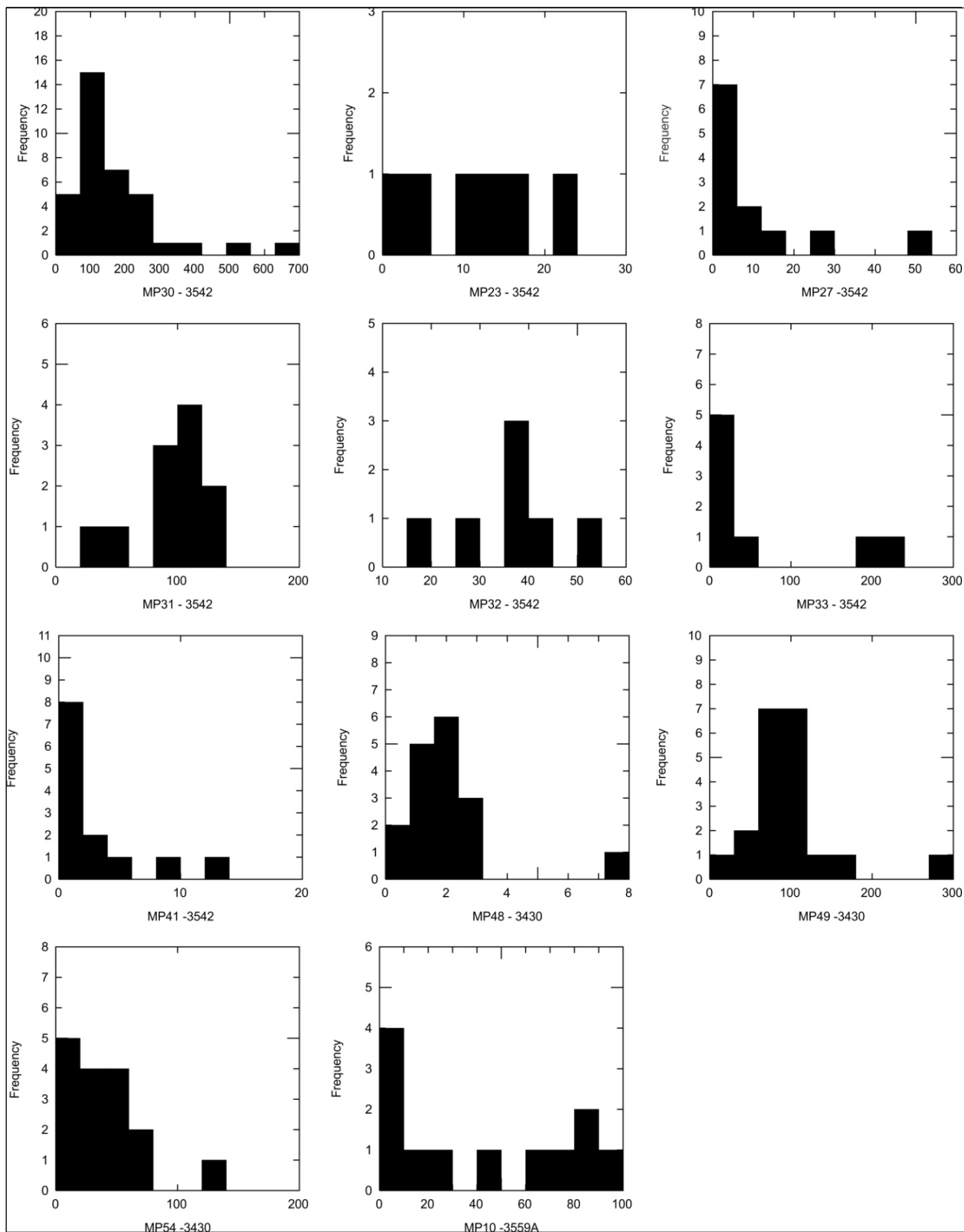


Figure 16: Histograms for gold distribution in pyrite, divided by sample from LA-ICP-MS data, demonstrating the wide spread of values both within and between samples. Scale is in ppm.

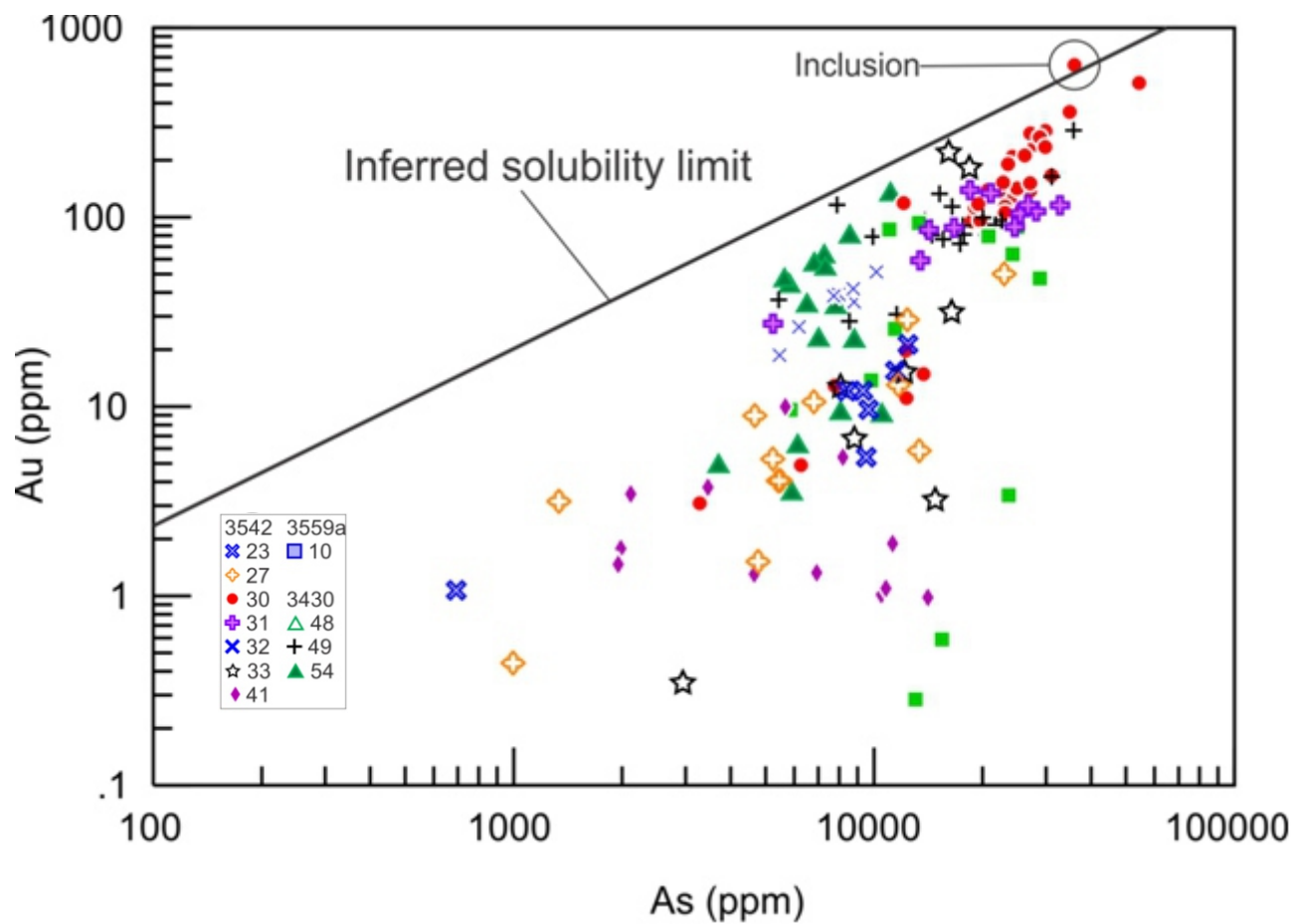
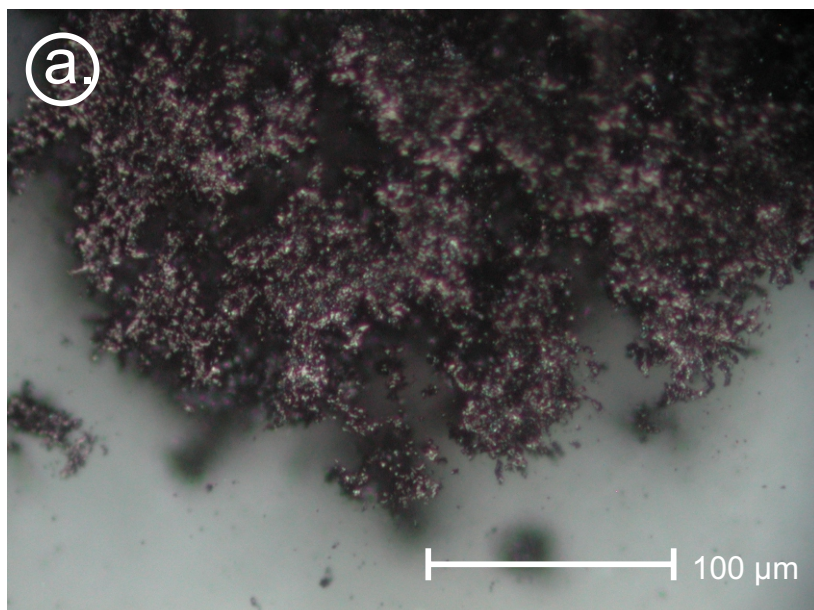
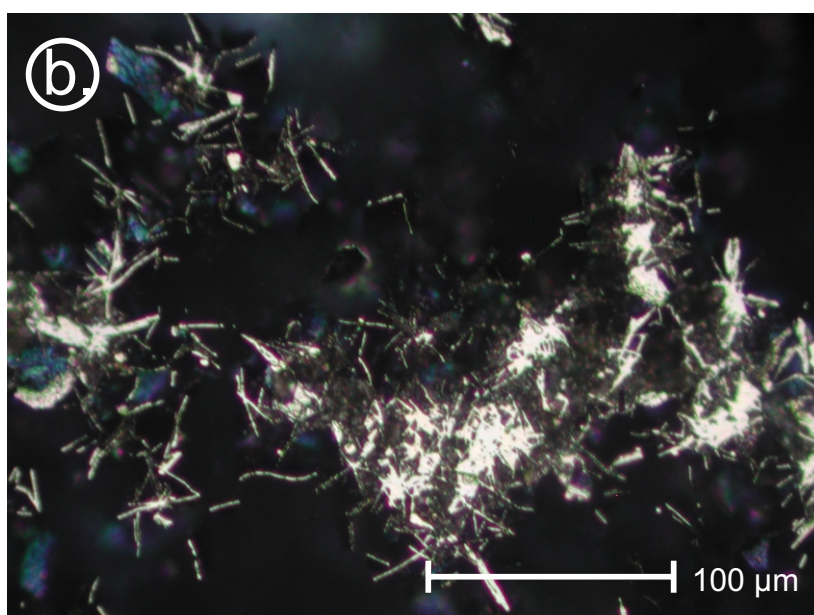


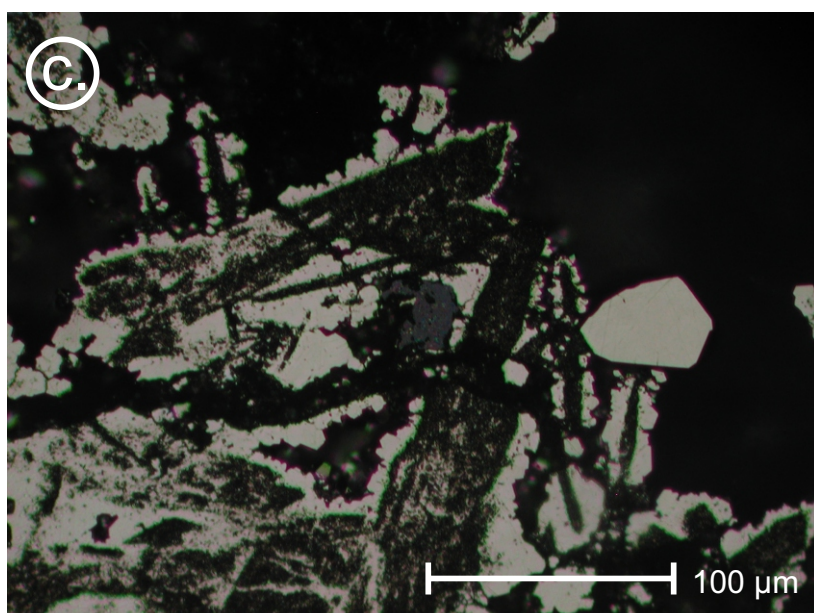
Figure 18: Summary plot of all LA-ICP-MS spot analysis of pyrite expressed as Au vs. As. The inferred solubility limit for Au in pyrite (Reich et al. 2005) is approximated by the line $C_{Au} = 0.02 \times C_{As} + 4 \times 10^{-5}$, where C_{Au} and C_{As} represent the concentration of Au and As in ppm. Below the line, Au can be present in solid solution (Au^{+1}), whereas above, a component of Au is present as inclusions (Au^0).



End member
Molybdenite



Intermediate



End member
Pyrite replacement

Figure 19: Reflected light photo-micrographs of a) Molybdenite; b) pyrite intergrowths and c) 'dirty' textured pyrite with idiomorphic overgrowths.

Sample	Au (ppm)	Au-Rp1	Ag (ppm)	As (ppm)	Cu (ppm)	Mo (ppm)	Pb (ppm)	Sb (ppm)	Se (ppm)	Te (ppm)	Zn (ppm)
JMRD3559a											
2	0.20		0.70	714	27	<mdl	7.00	21	3.00	0.20	65
10	0.52		0.30	88	25	6.00	<mdl	17	<mdl	0.20	44
15	0.86	0.89	0.60	119	15	<mdl	<mdl	11	4.00	0.80	28
17	0.24		0.50	47	18	<mdl	7.00	7.70	<mdl	0.20	47
18	0.14		0.30	101	10.00	<mdl	<mdl	10.00	<mdl	<mdl	58
JMRD3542											
21	0.33		0.50	331	13	<mdl	<mdl	16	<mdl	0.20	35
39	0.51		1.30	203	12	3.00	<mdl	30	3.00	0.20	16
41	0.05		0.90	238	40	<mdl	7.00	8.89	<mdl	0.10	124
43	4.25	4.08	3.20	756	38	<mdl	5.00	18	2.00	0.10	40
JMRD3542											
46	56	54	14	<mdl	17	3.00	<mdl	5.83	<mdl	3.00	10.00
58	1.94	2.05	2.10	172	57	<mdl	<mdl	21	<mdl	0.20	47
Detection limit	0.01	-	0.20	10.00	1.00	2.00	5.00	0.05	2.00	0.1	1
Method	FA/AAS	-	AMS	AOES	AOES	AOES	AOES	AMS	AMS	AMS	AOES

Methods: FA/AAS – 25g Lead collection fire assay, Flame Atomic Absorption Spectrometry; AMS – ICP-MS analysis of multi-acid digest (HF, HNO₃, HClO₃, HCl); AOES ICP (Optical) Atomic Emission Spectrometry of multi-acid digest. Genalysis Laboratory Services, Adelaide.

Table 1: Assay data

Sample	Au	Ag	Hg	Cu	Bi	Te	Total
ag1	29.20	68.94	3.13	0.01	0.15	-	101.43
ag3re	16.68	79.42	4.95	-	0.02	0.07	101.14
ag5	-	99.78	0.01	0.06	0.04	0.11	100.01
ag12	27.70	68.92	3.37	-	-	0.07	100.06
ag13	42.10	58.64	1.11	0.04	0.23	0.15	102.27
ag14	7.60	92.25	0.35	-	0.03	0.05	100.29
ag21	0.07	99.46	0.10	0.07	0.15	0.12	99.97
63mp1	72.31	28.75	-	-	-	0.03	101.09
49mp1	64.82	36.07	0.58	-	0.08	0.02	101.57
49mp2	67.05	32.73	0.81	-	-	0.12	100.71
49mp3	65.36	29.69	0.93	0.07	0.21	-	96.27
49mp5	64.17	33.82	0.54	-	0.27	0.11	98.90
34mp1	67.30	32.10	-	0.05	0.10	0.01	99.55
34mp2	68.48	33.37	-	0.06	0.07	0.05	102.02
35mp5	58.57	37.36	0.74	0.08	0.05	0.03	96.84
33mp66	64.81	37.13	0.80	0.04	0.08	0.03	102.88
33mp67	65.49	36.29	0.75	-	0.12	0.03	102.68
33mp68	64.51	36.16	0.47	-	0.17	-	101.31
33mp70	65.57	29.00	0.63	0.05	0.36	0.02	95.63

Table 2: EMPA data for electrum in wt%.

Sample	Mineral	Cu	Ag	Fe	Sb	As	S	Se	Total
MP88	Acanthite	<mdl	84	<mdl	<mdl	<mdl	16	<mdl	101.61
8MP10	Acanthite	<mdl	85	<mdl	<mdl	<mdl	16	1.09	101.95
8MP22	Acanthite	<mdl	84	<mdl	<mdl	<mdl	16	1.25	101.65
8MP23	Acanthite	<mdl	82	<mdl	<mdl	<mdl	15	1.19	99.12
8MP25	Acanthite	<mdl	84	<mdl	<mdl	<mdl	16	<mdl	101.46
8MP42	Acanthite	<mdl	83	<mdl	<mdl	<mdl	14	1.62	98.97
23mp13	Naumannite	<mdl	70	<mdl	2.07	<mdl	2.99	21	96.5
23mp17	Naumannite	<mdl	65	<mdl	1.48	<mdl	1.70	27	95.83
8MP2	Polybasite-pearcerite - low S	2.86	76	<mdl	5.25	2.17	12	<mdl	98.68
8MP4	Polybasite-pearcerite - low S	3.05	77	<mdl	5.76	2.03	13	<mdl	101.08
8MP15	Polybasite-pearcerite - low S	3.11	76	<mdl	4.89	2.44	13	<mdl	99.65
8MP16	Polybasite-pearcerite - low S	3.19	75	<mdl	5.36	2.15	12	1.40	99.26
8MP19	Polybasite-pearcerite - low S	3.39	74	<mdl	4.91	2.81	13	<mdl	99.87
8MPpts4	Polybasite-pearcerite	3.18	74	<mdl	5.37	2.57	14	<mdl	100.35
8MP20	Polybasite-pearcerite	3.21	74	<mdl	4.59	3.16	14	<mdl	99.82
8MP18	Polybasite-pearcerite	2.63	73	<mdl	6.59	2.38	15	<mdl	100.19
8MPpts1	Polybasite-pearcerite	3.37	72	<mdl	4.92	2.96	14	1.43	98.51
8MPpts2	Polybasite-pearcerite	3.00	71	<mdl	6.54	2.52	15	<mdl	98.81
8MPpts3	Polybasite-pearcerite	2.71	72	<mdl	6.92	2.50	15	<mdl	100.09
8MP45	Polybasite - low S	2.65	79	<mdl	4.65	2.41	12	<mdl	101.56
8MP11	Polybasite - low S	3.31	77	<mdl	5.08	2.39	12	<mdl	101.12
8MP14a	Polybasite - low S	2.66	78	<mdl	5.49	1.87	12	1.00	100.41
8MP27	Polybasite-pearcerite	3.60	73	<mdl	5.48	2.62	15	<mdl	100.39
8MP28	Polybasite-pearcerite	3.69	72	<mdl	6.07	2.31	14	<mdl	99.69
8MP30	Polybasite-pearcerite	3.17	74	<mdl	5.10	2.70	15	<mdl	100.39
8MP32	Polybasite-pearcerite	2.66	73	<mdl	5.21	2.56	15	1.05	98.76
8MP34	Polybasite-pearcerite	3.32	73	<mdl	6.34	2.11	14	1.24	99.72
8MP35	Polybasite-pearcerite	3.12	72	<mdl	5.49	2.94	15	1.03	99.93
8MP36	Polybasite-pearcerite	1.88	76	<mdl	8.89	<mdl	13	1.93	102.3
8MP37	Polybasite-pearcerite	3.07	74	<mdl	6.05	2.85	15	1.18	102.15
8MP38	Polybasite-pearcerite	2.90	72	<mdl	8.72	<mdl	13	2.83	101.06
8MP39	Polybasite-pearcerite	1.93	72	<mdl	10	<mdl	14	1.77	100.96
8MP40	Polybasite-pearcerite	3.13	72	<mdl	6.23	2.52	15	1.13	100.19
8MP41	Polybasite-pearcerite	3.17	73	<mdl	6.30	2.53	15	1.11	101.45
8MP43	Polybasite-pearcerite	2.88	74	<mdl	6.54	1.94	14	<mdl	100.54
8MP11	Polybasite - missing As	3.31	77	<mdl	5.08	<mdl	12	<mdl	98.73
8MP12	Polybasite - missing As	2.31	83	<mdl	4.95	<mdl	11	<mdl	101.8
8MP13	Polybasite - missing As	3.02	78	<mdl	5.39	<mdl	13	<mdl	100.28
8MP13a	Polybasite - missing As	2.55	82	<mdl	4.67	<mdl	11	<mdl	100.21
8MP14	Polybasite - missing As	3.13	76	<mdl	6.07	<mdl	13	<mdl	98.79
23mp12	Pyragyrite	<mdl	61	<mdl	20	<mdl	16	2.11	100.52
23mp17	Pyragyrite	<mdl	59	<mdl	21	1.82	17	<mdl	100.4
23mp8	Ag-rich tetrahedrite	15	31	4.23	24	1.50	20	<mdl	96.49
35mp7	Ag-rich tetrahedrite	15	31	4.26	24	1.49	20	<mdl	96.94
8MP19	Ag-rich tetrahedrite	16	30	4.43	23	1.96	20	<mdl	95.61

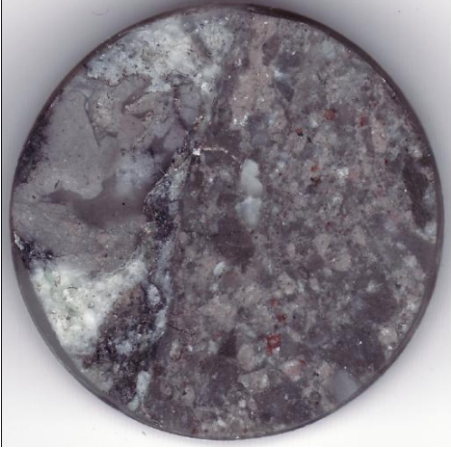
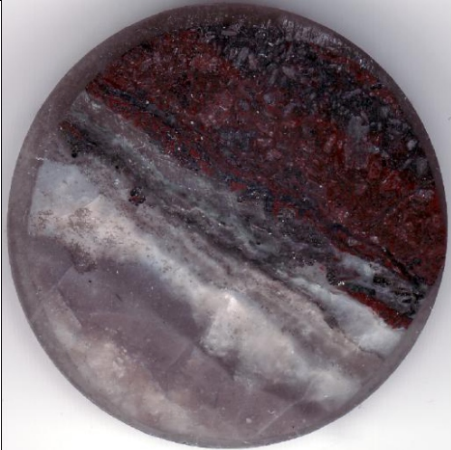

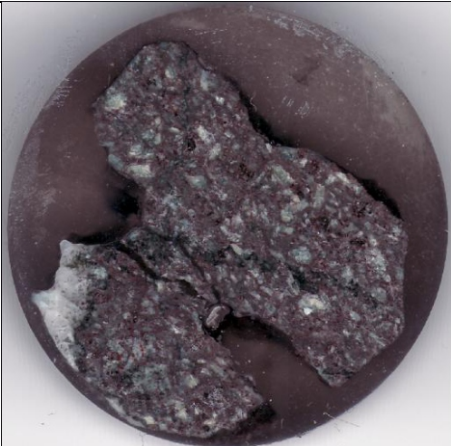
Table 3: Summary of EMPA data on silver minerals

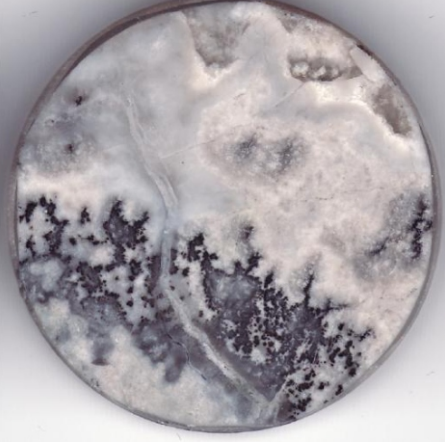
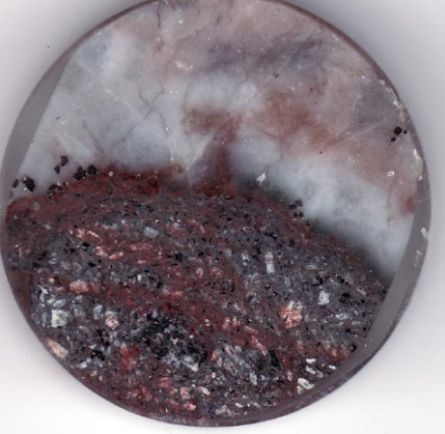


Sample/Texture	Au (ppm)	As (ppm)	Ag (ppm)	Sb (ppm)	Se (ppm)	Mo (ppm)	Tl (ppm)	Cu (ppm)	Co (ppm)	Ni (ppm)	Number of analyses
<i>MP30 - 3542</i>											
Clean (alteration)	76	17763	172	282	78	549	22	470	958	478	8
Clean (vein)	215	24815	164	230	128	889	19	767	14	41	18
Dirty (vein)	157	25926	1390	1343	128	12856	209	635	112	457	10
<i>MP31 - 3542</i>											
Clean (alteration)	85	16098	201	408	87	2153	39	147	16	84	3
Dirty lamellar (vein)	97	23577	824	1563	124	9283	173	424	89	328	5
Overgrowth (vein)	108	20267	969	1239	89	13944	128	412	86	327	3
<i>MP32 - 3542</i>											
"Blady" (vein)	36	7873	648	904	77	3888	85	317	0.18	0.50	7
<i>MP33 - 3542</i>											
Idiomorphic, Siciliclastics (alt)	12	10536	73	630	23	0.57	25	524	75	66	6
Idiomorphic (vein)	182	18389	61	78	72	2.62	0.56	890	12	30	1
<i>MP49 -3430</i>											
Idiomorphic (vein)	101	19447	121	144	205	147	13	249	0.12	2.79	13
Wispy (vein)	97	10555	284	400	121	771	31	321	0.37	0.48	2
<i>MP54 -3430</i>											
Clean (alteration)	19	7407	92	121	66	22	5.02	594	903	463	3
Feathery (vein)	45	7294	357	686	121	316	26	198	49	20	12
<i>MP10 -3559A</i>											
Large brecciated grain (alt.)	42.59	16,878.16	38.33	157.37	49.26	0.33	14.28	404.79	113.00	16.90	12

Table 4: Summary of LA-ICP-MS data for pyrite; means values for textures grouped by sample.



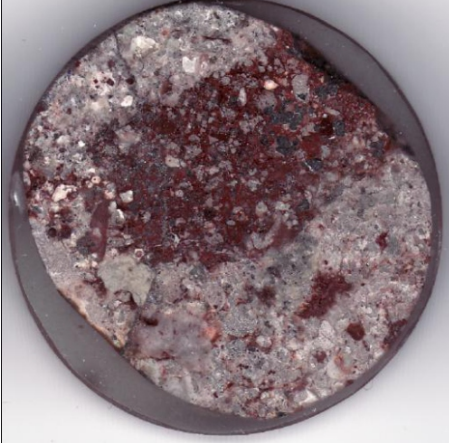

Appendices


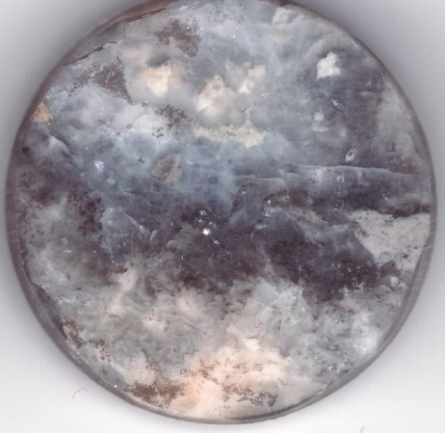
Appendix 1: Table of samples49
Appendix 2: XRD diffractograms.....54
Appendix 3: Total dataset for EMPA data in pyrite55
Appendix 4: Total dataset for LA-ICP-MS data in pyrite60

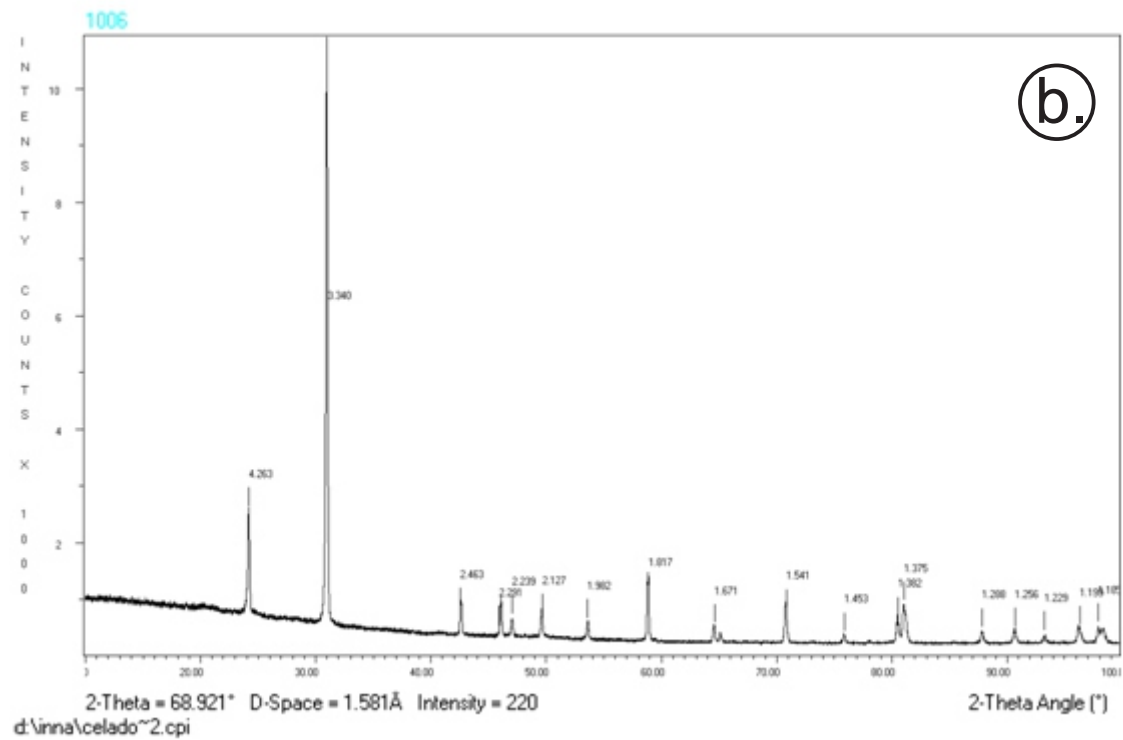
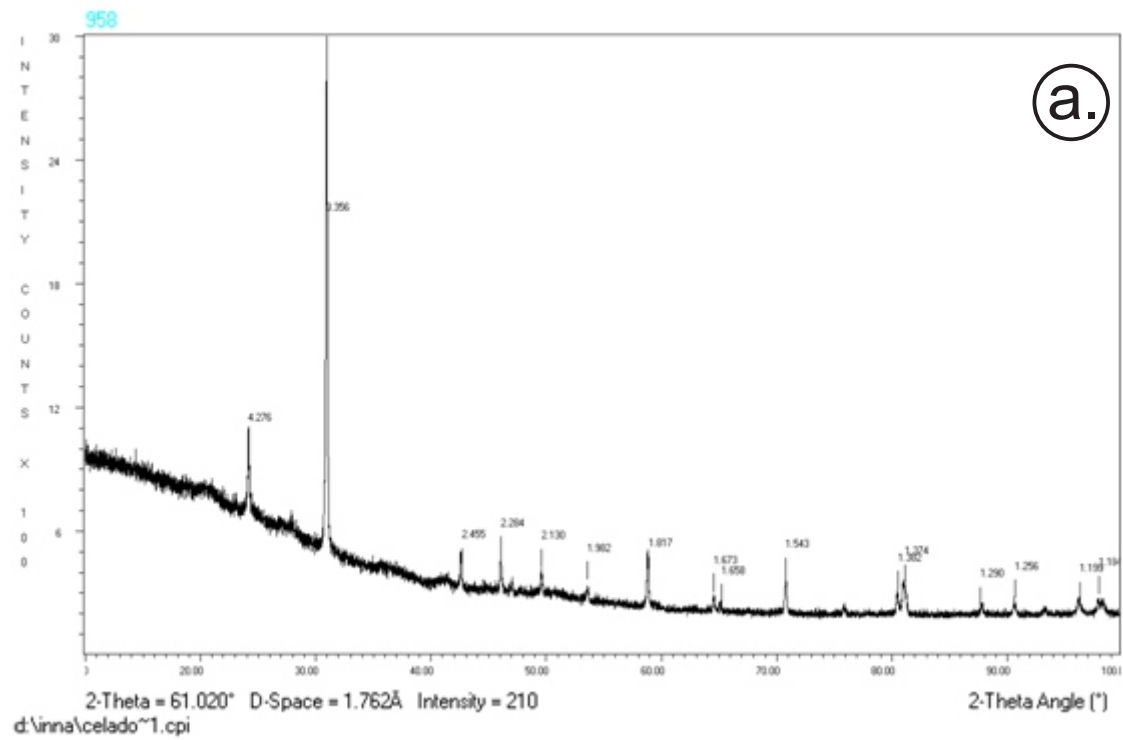
Sample/ Drill core		Depth (m)	Description
JMRD3559a MP8		645.8	Silicified andesite host rock with silica vein. Silver mineral in vein, minor pyrite.
MP10		664	Hematite altered andesite adjacent to chalcedonic quartz vein with pyrite.
MP11		661	Chalcedonic quartz.
MP12		680	Silicified andesite breccia; chalcopryrite polished out of sample.

MP13		683.3	Vuggy chalcedonic quartz.
MP16		657.37	Hematite altered andesite adjacent to chalcedonic quartz vein with pyrite.
JMRD3542			
MP27		435.2	Haematite altered andesite breccia with sulphide bearing silica vein.
MP29		448.1	Haematite altered andesite with chalcedonic quartz vein.

MP32		448.2	Pseudomorphed blady quartz after calcite, with bladed pyrite.
MP33		431	Siliclastic sediments, altered with green chalcedonic quartz, with a vuggy, pyrite bearing black banded silica vein.
MP34		457.6	Silicified multiphase argillic breccia with black silica vein.
MP35		457.7	Quartz veining in quartz loded andesitic volcanic breccia.

MP41		479.7	Propylitic altered andesite with evenly distributed pyrite.
MP43		483.65	Silicified propylitic andesite breccia with minor siderite veins.
JMRD3430			
MP48		419.45	Haematite, pyrite bearing clast in silicified andesite breccia.
MP49		447.8	Wispy pyrite in black silica band in crustiform vein.

MP54		455.3	Feathery textured pyrite in silica vein around silica/argillic altered andesite clast.
JMRD3253			
MP52		601.5	Chalcedonic quartz.



Appendix 2: XRD diffractograms on green chalcedony from Mp33 from drillcore JMRD 3542 for a) 30 minutes and b) 40 minutes. Both spectra indicate quartz.

Label	S	Mn	Fe	Co	Ni	Cu	As	Se	Sb	Total
29mp1	54.54	-	45.67	-	0.05	0.06	0.18	0.05	0.01	100.56
29mp1	53.62	0.01	46.1	-	0.02	0.05	1.18	-	0.09	101.07
23mp10	54.08	-	46.59	0.09	0.03	-	0.27	0.06	0.01	101.12
29p1	53.67	-	46.87	-	0.02	0.06	-	-	0.01	100.62
29p2	54.11	-	46.76	-	0.02	0.04	-	-	0.12	101.06
29p3	53.55	-	46.69	-	-	0.04	0.84	-	0	101.13
29p5	53.94	-	46.35	0.06	-	-	0.51	0.02	0.05	100.93
29p6	53.32	0.01	46.71	-	-	0.03	1.06	0.08	0.04	101.24
29p7	53.83	0.02	45.98	-	0.02	0.13	0.74	0.06	0.3	101.09
29p8	52.48	-	45.56	-	0.05	0.04	0.78	-	0.06	98.97
29p9	53.4	-	46.62	-	0.03	-	1.36	0.04	0	101.46
29p10	52.55	0.02	45.86	-	0.01	0.05	2.87	0.07	0	101.42
29p12	53.89	-	46.67	-	0.06	0.06	0.69	0.04	0	101.42
29p13	54.08	-	46.73	0.05	-	0.06	0.57	-	0	101.49
29p16	52.27	0.04	45.24	-	-	0.01	0.43	0.08	0.01	98.08
29p17	52.47	-	47.04	-	0.04	-	2.92	0.02	0.03	102.52
29p18	52.8	-	46.3	0.01	0.01	-	1.48	-	0.04	100.64
29p19	53.8	-	46.69	-	0.02	0.02	0.74	-	0	101.26
29p20	53.55	-	46.89	0.01	0.1	0.02	0.94	0.02	0.05	101.57
29i1_1	52.38	0.01	46.07	-	-	-	3.31	0.08	0.03	101.9
29i1_2	51.73	0.02	46.45	-	-	0.04	3.57	-	0	101.81
29i1_3	51.95	0.03	46.35	-	-	-	3.57	0.09	0.01	101.99
29i1_4	54.19	-	47.63	-	0.02	0.03	0.69	-	0	102.56
29i1_5	54.4	-	47.2	-	0.02	-	0.3	-	0	101.91
10mp21	52.59	0.01	46.54	-	0.05	-	1.73	0.1	0.01	101.02
10mp22	51.93	0.02	46.88	-	-	0.01	2.38	0.07	0	101.29
10mp23	53.87	-	47.3	-	-	0.02	0.37	0.04	0.06	101.65
10mp24	53.26	0.02	46.32	-	-	0.02	1.42	-	0.08	101.11
10i2_1	53.76	0.03	46.28	-	-	0.01	1.06	0.06	0.03	101.22
10i2_2	53.78	0.02	46.63	-	0.04	-	1.19	0.15	0.03	101.84
10i2_3	54.33	-	46.75	-	0.01	0.01	0.53	-	0.03	101.67
10i2_4	53.43	-	46.43	-	0.03	0.05	1.67	-	0.01	101.62
10i2_5	53.72	-	46.2	-	0.02	0.02	1.04	-	0.06	101.06
10i2_6	53.63	0.03	46.45	-	-	0.01	1.14	-	0	101.26
10i2_7	53.77	-	46.6	-	-	-	1.02	0.06	0.09	101.55
10mp26	52.94	-	46.61	0.03	0.02	0.01	2.19	0.06	0	101.87
10mp25	52.99	0.02	46.48	0.01	0.03	-	2.77	0.02	0.06	102.38
10mp27	54.45	-	47.33	-	-	-	0.01	0.07	0	101.87
10mp28	54.12	-	47.38	-	0.01	-	0.11	0.01	0.1	101.72
10mp29	52.66	-	46.33	-	-	0.08	2.49	0.02	0.02	101.6
10mp30	54.76	0.03	47.28	0.02	-	-	0.07	0.05	0.11	102.32
10mp31	54.65	0.01	46.91	-	0.01	0.06	0.11	0.14	0.03	101.92
10mp32	52.51	-	46.86	-	0.01	-	2.33	0.01	0	101.72
10mp33	54.28	0.03	47.71	-	-	-	0.23	-	0	102.26
10mp34	54.03	-	47.21	0.02	-	0.03	0.94	0.05	0.09	102.37

Appendix 3: EPMA data for pyrite in wt%.

Label	S	Mn	Fe	Co	Ni	Cu	As	Se	Sb	Total
10mp35	52.97	-	46.33	-	0.04	-	2.14	0.02	0.03	101.53
10mp36	52.46	-	46.59	-	0.06	-	2.84	0.02	0.05	102.01
10mp37	53.15	-	47.24	-	0.01	-	1.62	0.01	0.12	102.15
10mp38	52.33	-	47.01	-	-	0.04	2.91	0.07	0.03	102.39
10mp39	54.02	0.01	46.91	-	0.03	-	0.91	0.07	0.02	101.97
10mp40	53.31	-	46.97	-	0.03	0.01	1.66	-	0.01	101.97
35mp41	51.69	0.04	46.24	-	-	0.03	3.39	0.03	0.00	101.41
35mp42	52.80	-	46.64	0.03	0.01	-	2.69	0.02	0.03	102.21
35mp43	52.15	-	46.58	-	0.02	-	3.32	0.09	0.06	102.23
35mp44	52.24	0.01	46.37	-	0.05	0.03	2.56	0.02	0.08	101.37
35mp45	53.60	-	46.79	0.01	-	0.05	1.10	0.05	0.03	101.64
35mp46	52.52	-	46.25	-	0.06	0.11	2.98	0.08	0.00	102.00
35mp47	51.83	-	46.63	-	0.03	0.06	3.34	0.11	0.03	102.04
35mp48	54.29	-	47.56	-	-	0.04	0.19	0.04	0.00	102.12
35mp49	52.51	-	46.18	-	-	0.02	2.66	0.01	0.00	101.39
35mp50	53.73	-	47.04	-	0.03	-	0.75	0.02	0.00	101.57
35mp51	53.37	-	46.73	0.01	-	0.04	1.68	0.09	0.01	101.93
35mp52	54.13	-	47.01	-	0.01	0.01	0.16	0.08	0.03	101.44
35mp53	53.40	-	46.25	-	-	0.10	0.95	-	0.01	100.70
35i3_1	54.24	0.01	46.91	-	-	0.05	0.28	0.01	0.00	101.51
35i3_2	52.67	0.01	46.88	-	-	0.02	1.77	-	0.06	101.40
35i3_3	53.63	-	46.97	-	0.04	0.03	1.02	0.07	0.04	101.81
35i3_4	53.80	-	47.20	-	0.02	0.05	0.52	0.01	0.00	101.60
35mp55	52.59	-	46.63	-	0.02	0.01	2.75	0.07	0.07	102.14
35mp56	54.73	0.01	47.04	-	-	-	0.17	0.07	0.02	102.04
35mp57	51.13	-	46.10	-	0.05	0.08	4.24	0.01	0.00	101.61
35mp58	51.19	-	46.20	-	0.04	0.03	3.96	0.06	0.05	101.53
35mp59	51.94	-	46.49	-	-	0.04	3.00	0.05	0.05	101.57
35mp60	51.89	-	46.22	-	0.02	0.02	3.46	0.04	0.04	101.69
35mp61	52.17	-	46.43	-	0.01	0.02	3.14	0.12	0.03	101.93
35mp62	52.10	-	46.83	-	-	0.08	3.15	0.09	0.00	102.26
33mp63	53.47	0.01	46.79	0.01	-	0.07	0.76	0.04	0.02	101.16
33mp65	54.51	-	46.82	-	0.05	0.05	0.12	-	0.09	101.63
33mp71	51.07	0.02	45.46	-	0.03	0.07	4.76	0.03	0.03	101.47
33mp72	51.30	0.01	45.96	-	0.02	0.15	4.31	0.10	0.00	101.87
33mp73	35.74	-	29.27	-	-	34.73	0.01	-	0.00	99.76
33mp74	53.72	0.02	46.87	-	-	0.02	0.62	-	0.07	101.32
33mp75	50.27	-	47.64	0.01	-	0.03	1.11	0.03	0.00	99.09
33mp76	54.28	0.02	47.31	-	-	-	0.28	-	0.00	101.89
33mp78	53.71	-	46.71	0.01	0.04	0.02	2.14	0.05	0.03	102.70
33mp79	53.11	0.01	46.41	-	0.01	0.04	1.94	0.02	0.00	101.54
33mp81	54.19	0.02	47.17	-	0.01	-	0.06	-	0.02	101.47
33mp80	53.97	0.01	47.16	-	-	0.07	0.17	0.06	0.01	101.45
33mp82	52.67	0.01	46.39	-	-	0.06	2.17	0.06	0.00	101.36
33mp83	52.77	-	46.45	0.01	-	0.06	2.15	0.02	0.00	101.45

Label	S	Mn	Fe	Co	Ni	Cu	As	Se	Sb	Total
33mp84	53.72	0.01	47.24	-	-	0.05	0.87	0.06	0.05	101.99
33mp85	51.18	0.02	46.01	-	-	0.11	3.76	0.06	0.05	101.19
33mp86	51.37	0.01	46.42	-	0.03	-	4.33	0.04	0.04	102.25
33mp87	53.01	0.03	46.54	-	-	-	1.33	-	0.01	100.93
33mp88	48.63	0.01	45.45	-	0.02	0.06	7.15	0.07	0.00	101.40
33mp89	52.43	-	45.87	-	-	-	2.42	-	0.00	100.72
33mp90	52.15	-	46.22	0.04	-	-	2.96	0.08	0.00	101.45
ag26	51.65	-	44.99	-	-	0.09	2.97	-	0.00	99.70
ag27	53.43	-	46.02	-	-	0.03	0.88	-	0.01	100.40
ag28	52.24	0.02	45.42	-	-	-	2.02	-	0.03	99.70
63mp2	52.23	0.03	45.48	-	-	0.02	2.46	0.05	0.00	100.30
63mp3	51.32	0.01	44.10	-	0.02	0.02	3.34	0.08	0.03	98.90
63pt1	51.77	-	46.28	-	0.01	-	2.18	0.03	0.03	100.30
63pt2	52.94	0.01	46.45	0.02	0.03	0.03	0.66	-	0.00	100.20
63pt3	53.32	0.02	47.15	0.03	-	-	1.04	0.08	0.03	101.70
63pt4	52.34	-	46.73	0.03	-	0.03	2.51	0.05	0.09	101.80
63pt5	52.22	0.01	46.12	-	-	-	3.15	0.01	0.00	101.50
63pt6	51.96	0.01	45.80	-	-	-	2.94	0.01	0.05	100.80
63pt7	53.07	0.02	45.55	-	-	0.02	1.93	-	0.04	100.60
63pt8	52.21	-	45.83	-	0.05	-	3.44	0.04	0.03	101.60
63pt9	50.94	-	44.48	-	-	0.03	4.80	0.43	0.00	100.70
63pt10	53.94	-	46.66	-	0.05	-	0.51	-	0.01	101.20
63pt11	52.24	-	45.64	-	-	0.02	2.03	-	0.03	100.00
63pt12	52.93	-	45.27	-	-	-	1.58	0.01	0.04	99.80
63pt13	53.87	-	46.18	0.02	-	0.03	0.15	-	0.00	100.20
63pt14	53.43	-	45.74	-	0.02	-	0.66	-	0.04	99.90
63pt15	51.54	0.02	45.22	-	0.02	0.02	3.40	-	0.09	100.30
63pt16	51.13	-	45.63	-	-	0.01	3.39	0.03	0.06	100.30
63pt17	52.20	0.02	44.93	-	-	0.01	2.77	-	0.10	100.00
63pt18	51.96	-	45.40	-	0.02	0.01	3.16	-	0.00	100.60
63pt19	51.78	0.01	45.33	-	0.05	-	3.22	0.06	0.04	100.50
63pt20	52.00	-	45.92	-	0.02	0.04	2.12	-	0.00	100.10
63pt21	53.87	-	46.09	-	0.02	-	0.43	0.04	0.03	100.50
49pt22	53.34	-	46.37	-	-	0.06	1.26	0.02	0.05	101.10
49pt23	53.21	-	45.83	-	0.03	0.02	1.39	0.02	0.07	100.60
49pt24	52.57	-	45.78	-	0.02	-	2.71	0.04	0.05	101.20
49pt25	53.86	0.02	45.71	-	-	0.05	0.26	0.04	0.00	99.90
49pt26	53.76	-	45.75	-	0.01	-	0.07	0.09	0.19	99.90
49pt27	53.50	-	45.51	-	-	0.02	0.71	0.01	0.04	99.80
49pt28	51.67	-	45.09	-	-	-	3.34	0.05	0.16	100.30
49pt29	51.77	0.01	45.57	0.01	-	0.06	3.22	0.01	0.01	100.70
49pt30	51.35	-	45.22	-	0.04	0.10	3.75	-	0.04	100.50
49pt31	51.77	0.01	45.78	-	0.01	0.12	3.63	-	0.07	101.40
49pt32	53.41	-	45.82	-	0.03	0.08	0.65	-	0.04	100.00
30pt33	52.14	0.02	45.81	-	-	0.01	2.85	-	0.05	100.90

Label	S	Mn	Fe	Co	Ni	Cu	As	Se	Sb	Total
30pt34	51.90	-	45.72	-	0.04	0.10	3.13	-	0.08	101.00
30pt35	51.74	0.01	45.55	-	-	0.07	2.95	-	0.06	100.40
30pt36	52.52	0.01	46.25	-	0.01	0.05	2.80	-	0.03	101.70
30pt37	53.26	-	46.19	-	-	-	1.56	-	0.02	101.00
30pt38	52.03	0.01	46.01	-	0.01	-	2.61	-	0.08	100.70
30pt39	53.94	0.01	46.39	-	-	-	0.16	-	0.04	100.60
30pt40	54.27	0.03	46.60	0.02	0.02	0.14	0.27	-	0.00	101.40
3011_1	52.23	-	45.54	-	-	0.03	2.16	-	0.02	100.00
3011_2	52.12	-	45.81	-	0.02	-	3.02	-	0.04	101.00
3011_3	52.69	-	45.54	-	0.05	0.08	2.34	0.04	0.00	100.80
3011_4	51.81	0.01	45.41	-	-	0.03	3.44	-	0.07	100.80
3011_5	52.18	0.01	45.64	-	0.03	-	2.70	-	0.05	100.60
3012_1	52.16	-	45.95	-	0.01	0.02	2.77	0.01	0.00	100.90
3012_2	52.25	-	45.91	-	-	0.06	2.59	0.02	0.01	100.80
3012_3	52.11	0.02	46.12	-	0.03	-	3.09	-	0.03	101.40
3012_4	51.88	-	46.31	-	-	0.01	3.08	0.06	0.09	101.40
3012_5	52.02	-	46.13	-	-	0.05	3.28	-	0.09	101.60
3013_1	54.90	-	46.34	-	-	-	0.02	-	0.00	101.30
3013_2	52.40	0.01	45.78	-	0.03	0.09	2.26	0.07	0.03	100.70
3013_3	52.74	-	45.75	0.04	0.03	0.03	2.20	-	0.06	100.90
3013_4	51.66	-	45.61	-	-	-	3.74	-	0.06	101.10
3013_5	52.42	-	45.73	-	0.03	0.04	3.35	0.01	0.04	101.60
3014_1	51.69	-	45.59	-	0.01	0.01	2.29	-	0.00	99.60
3014_2	54.28	-	46.80	0.01	0.03	0.02	0.31	-	0.00	101.50
3014_3	53.30	0.02	46.15	-	-	0.04	1.73	-	0.04	101.30
30pt41	53.99	-	46.04	-	-	0.08	1.04	0.05	0.02	101.20
30pt42	52.81	-	46.04	-	-	-	2.25	0.01	0.06	101.20
30pt43	52.79	-	46.03	-	0.03	0.02	1.95	0.03	0.00	100.90
30pt44	51.41	0.03	45.73	-	-	0.07	3.72	-	0.00	101.00
34pt45	53.66	-	46.41	-	0.01	0.02	0.65	0.08	0.00	100.80
34pt46	54.07	0.01	46.68	-	0.06	-	0.08	-	0.01	100.90
34pt47	53.52	-	44.07	0.01	-	0.02	0.36	0.08	0.00	98.10
34pt48	53.78	-	44.39	-	0.03	0.02	0.17	0.05	0.00	98.40
34pt49	52.01	-	44.10	0.20	0.22	-	2.45	-	0.00	99.00
34pt50	53.68	0.01	44.94	-	0.01	0.12	0.02	0.07	0.00	98.90
4111_1	53.83	-	46.76	-	0.02	0.02	0.24	0.03	0.03	100.90
4111_2	53.85	-	46.36	-	-	-	0.45	0.06	0.01	100.70
4111_3	53.84	-	46.18	-	0.04	-	0.57	-	0.01	100.60
41pt51	53.76	0.01	46.57	-	-	0.02	0.31	-	0.00	100.70
41pt52	53.71	-	45.42	-	0.01	0.24	0.77	0.05	0.10	100.30
41pt53	52.94	0.01	45.04	-	0.01	0.04	1.44	-	0.02	99.50
41pt54	54.16	-	45.12	-	0.02	-	0.12	-	0.02	99.40
41pt55	54.10	-	46.49	-	0.02	0.02	0.34	0.04	0.02	101.00
41pt56	53.22	0.02	46.06	-	-	0.03	1.31	0.07	0.00	100.70
41pt57	54.20	0.01	46.24	-	0.02	0.02	0.42	-	0.03	100.90

Label	S	Mn	Fe	Co	Ni	Cu	As	Se	Sb	Total
41pt58	53.94	0.01	46.38	-	0.01	0.01	0.72	0.01	0.01	101.10
41pt59	52.50	-	45.89	0.02	-	0.09	2.28	0.04	0.09	100.90
41pt60	53.54	0.01	45.65	0.01	0.01	0.07	0.72	-	0.06	100.10
41pt61	53.44	0.01	46.31	-	-	-	1.13	-	0.05	100.90
41pt62	53.07	0.03	45.97	-	0.03	0.03	2.07	0.01	0.03	101.20
41pt63	53.92	-	45.88	0.12	0.04	-	0.44	0.04	0.00	100.40
41i2_1	54.02	-	46.24	0.03	-	0.03	0.37	-	0.00	100.70
41i2_2	53.13	-	46.41	-	0.02	0.08	0.50	0.05	0.07	100.30
41i2_3	53.84	-	46.60	0.01	0.02	0.08	0.54	-	0.01	101.10
41i2_4	53.84	0.01	46.44	0.01	0.04	-	0.72	-	0.00	101.10
41i2_5	53.32	0.01	45.91	-	-	0.06	0.67	0.05	0.01	100.00
41i2_6	53.95	-	46.26	0.08	0.02	-	0.34	0.01	0.00	100.70
41i2_7	54.15	-	46.61	0.02	0.03	0.03	0.38	0.05	0.00	101.30
41i2_8	53.42	0.02	45.89	0.01	-	0.01	1.29	-	0.05	100.70
41i2_9	53.88	0.03	46.54	0.03	0.01	-	0.73	-	0.02	101.20
41i2_10	54.19	-	46.04	-	-	-	0.10	0.05	0.00	100.40

Sample/Texture	Au (ppm)	Au precision (ppm)	Au mdl (ppm)	As (ppm)	Ag (ppm)	Sb (ppm)	Se (ppm)	Mo (ppm)	Tl (ppm)	Cu (ppm)	Zn (ppm)	Co (ppm)	Ni (ppm)
<i>MP30 - 3542</i>													
Clean, Vein, Core	4.91	5.23	0.04	6267	27	33	108	71	0.93	100	<mdl	56	83
Clean, Alteration	11	5.67	0.03	12302	115	121	89	4.63	3.62	340	1.13	244	124
Clean, Alteration	13	9.00	0.04	7779	69	182	51	2.72	4.03	1378	38	255	343
Clean, Alteration	15	9.95	0.03	13713	102	493	20	41	47	718	14	6651	2875
Large clean, grain bound., Alt.	20	11.66	0.05	12252	37	160	14	223	27	429	1.17	401	213
Dirty, Vein	95	5.29	0.02	18657	1447	939	122	11868	131	614	5.00	69	462
Large clean, Alteration	96	6.13	0.08	19699	101	109	79	753	10	166	1.37	55	76
Dirty, Vein	98	4.97	1.03	23776	1582	1050	144	22080	279	590	3.93	72	467
Clean, Alteration, Fractured	105	6.12	0.04	23083	116	66	122	1956	7.69	127	0.53	10	5.21
Dirty, Vein	106	4.97	1.27	24707	1927	1213	152	31619	473	663	4.05	73	432
Dirty, Vein	112	5.13	0.02	19038	1324	943	120	8761	173	664	6.71	131	497
Dirty, Vein	113	5.52	0.04	23094	1327	869	150	12968	132	549	1.42	102	473
Dirty, Vein	117	4.80	0.04	19459	1388	928	128	9653	239	673	4.34	135	511
Aggregate, Vein	119	7.19	0.04	12077	712	1984	133	2844	124	1235	5.66	35	102
Dirty, Vein	120	5.32	0.03	24091	702	743	129	8907	68	466	25	40	103
Clean, Vein	124	5.82	0.03	23773	24	24	118	9.43	0.15	663	27	<mdl	<mdl
Clean, Vein	134	5.53	0.04	21936	65	60	113	28	0.50	716	82	0.75	2.20
Large clean, grain bound., Alt.	138	5.93	0.03	27094	50	37	68	232	2.61	176	1.25	9.28	30
Clean, Vein	138	5.18	2.99	22240	112	88	116	1081	16	932	112	2.20	11
Clean, Vein	139	5.42	0.01	20698	67	75	113	4.35	0.74	1686	63	<mdl	1.20
Dirty, Vein	142	5.00	1.73	24942	915	1022	109	3244	89	583	3.03	62	415
Dirty, Vein	151	4.90	0.04	27102	1261	1453	131	13459	123	627	11	99	471
Clean, Vein	152	6.02	0.58	22816	55	49	147	11	0.35	1567	69	0.05	<mdl
Clean, Vein, Rim	166	5.40	0.03	31094	60	101	112	44	6.18	154	<mdl	5.91	1.86
Clean, Vein	188	5.57	0.03	23518	49	57	128	8.43	0.58	1247	54	1.73	0.94
Clean, Vein	190	6.31	0.03	23528	55	46	150	12	0.37	1444	62	0.06	0.15
Clean, Vein	209	6.07	0.02	24188	30	32	123	14	0.53	679	19	0.36	0.48
Aggregate, Alteration	212	6.85	13	26181	788	1087	180	1179	70	428	1.56	40	154
Aggregate, Vein	234	5.36	0.74	29857	1113	1427	116	7989	128	591	4.90	96	380
Clean, Vein, Fracture	241	5.99	0.02	27956	61	26	125	79	0.51	687	62	1.69	6.62
Clean, Vein	264	5.99	0.04	28841	9.78	5.57	135	8.23	0.04	373	1.79	0.35	0.54
Clean, Vein, Fracture	277	7.42	0.03	27145	37	31	117	154	0.44	218	0.83	0.90	7.92
Clean, Vein	285	7.33	0.03	29878	18	15	145	25	0.56	553	4.48	0.30	0.39
Clean, Vein	359	5.21	0.03	34879	5.91	3.75	161	6.61	<mdl	425	<mdl	0.07	<mdl
Dirty, Vein	511	5.07	0.02	54394	2027	4271	91	6004	378	921	8.15	338	736
Clean, Vein w/ electrum inc	636	11.13	1.82	35984	448	81	146	3615	51	542	0.60	18	18

Sample/Texture	Au (ppm)	Au precision (ppm)	Au mdl (ppm)	As (ppm)	Ag (ppm)	Sb (ppm)	Se (ppm)	Mo (ppm)	Tl (ppm)	Cu (ppm)	Zn (ppm)	Co (ppm)	Ni (ppm)
<i>MP23 - 3542</i>													
Small, Idiomorphic	1.07	8.06	0.04	693	120	381	11	<mdl	61	790	5.29	1875	489
Idiomorphic	5.40	8.76	0.03	9514	8.65	100	19	0.31	1.76	449	2.00	620	136
Small, Idiomorphic	9.61	11.33	0.04	9664	31	38	212	6.83	0.76	87	<mdl	243	78
Small, Idiomorphic	12	10.13	0.04	9316	20	149	43	0.11	7.14	416	1.31	168	47
Aggregate, Grain bound.	15	6.90	0.04	11466	98	78	80	12	1.13	190	16	61	79
Idiomorphic, Fracture	21	9.43	0.04	12431	84	45	14	0.23	1.01	2329	187	0.05	4.20
<i>MP31 - 3542</i>													
Clean, Alteration	27	15.53	0.04	5246	2.45	2.75	58	<mdl	0.02	16	<mdl	0.13	0.78
Dirty lamellar, Vein	59	10.76	0.03	13440	326	229	285	7059	50	382	1.27	93	99
Overgrowth, Vein	86	6.16	0.03	14215	1616	1104	97	24461	109	635	52	132	557
Dirty lamellar, Vein	88	5.77	0.05	16679	1203	1080	88	16319	156	517	37	91	430
Clean, Alteration	89	14.85	9.63	24572	476	1083	75	2953	94	271	17	24	214
Overgrowth, Vein	105	6.70	0.30	25491	921	1781	88	10785	202	428	15	90	374
Dirty lamellar, Vein, Black	107	5.88	2.61	28188	824	2113	85	7217	237	376	6.64	83	353
Dirty lamellar, Vein, Grey	115	5.91	0.40	32799	812	2394	84	5394	224	399	364	85	359
Dirty lamellar, Vein, Grey	116	5.85	0.02	26778	953	2001	77	10426	200	445	18	95	400
Overgrowth, Vein	134	6.14	0.04	21094	370	832	82	6585	75	172	5.15	35	50
Clean, Alteration	139	6.50	0.04	18475	125	137	129	1353	22	153	0.53	25	37
<i>MP27 -3542</i>													
Small, Idiomorphic	0.44	6.00	0.03	998	42	563	8.28	0.20	211	466	7.82	136	143
Small, Idiomorphic	1.52	4.07	0.05	4771	21	726	12	1.58	6.04	461	3.52	153	61
Small, Idiomorphic	3.16	4.50	0.10	1336	237	761	22	<mdl	4.30	2037	27	322	167
Subhedral, Core	4.05	8.12	0.04	5427	21	248	17	<mdl	142	235	3.29	103	36
Anhedral, Fracture	4.06	5.72	0.31	5498	40	132	118	1.10	10	366	8.31	179	86
Anhedral, Fracture	5.28	5.63	0.04	5237	29	352	34	1.15	7.69	309	3.98	341	161
Subhedral, Rim	5.84	6.15	0.04	13353	5.71	33	23	19	2.84	85	5.79	196	105
Small, Idiomorphic	8.94	10.97	0.03	4670	37	274	18	<mdl	18	515	16	1512	1228
Fractured	11	3.87	0.05	6813	51	69	199	26	6.71	333	3.16	21	32
Subhedral	13	9.03	0.03	11697	37	240	126	0.53	6.40	225	1.59	53	52
Small, Idiomorphic	29	7.43	0.04	12376	13	56	51	0.63	5.78	309	1.71	62	28
Flaky	50	5.39	0.04	22984	244	1008	30	146	26	180	108	8.74	185

Sample/Texture	Au (ppm)	Au precision (ppm)	Au mdl (ppm)	As (ppm)	Ag (ppm)	Sb (ppm)	Se (ppm)	Mo (ppm)	Tl (ppm)	Cu (ppm)	Zn (ppm)	Co (ppm)	Ni (ppm)
<i>MP48 - 3430</i>													
Large aggregate, Clean	0.36	8.34	0.04	4287	1.58	11	29	<mdl	0.07	311	0.55	26	63
Large grain, Rim	0.66	8.95	0.03	25389	19	13	<mdl	0.09	0.47	4.49	0.52	0.13	<mdl
Grain boundary	0.92	9.31	0.04	1154	43	35	22	0.09	0.57	230	6.30	222	73
Large aggregate, Porous	1.03	8.42	0.04	1229	0.36	60	<mdl	<mdl	0.67	112	1.86	16	7.92
Large aggregate, Rim	1.33	7.47	0.03	38111	13	32	3.25	0.18	3.01	12	0.94	0.09	0.19
Large aggregate, Porous	1.38	6.60	0.03	1595	8.15	113	<mdl	<mdl	2.04	128	4.32	21	11
Clean	1.45	9.43	0.07	34016	23	33	<mdl	<mdl	1.73	8.68	0.56	1.47	1.23
Aggregate, Core	2.05	6.05	0.03	4251	22	8.03	14	<mdl	0.27	55	<mdl	<mdl	<mdl
Large	2.06	8.19	0.04	18775	47	48	2.94	<mdl	2.28	6.99	<mdl	0.07	<mdl
Grain boundary	2.14	5.79	0.03	13636	108	165	12	<mdl	8.87	203	3.56	1.22	5.99
Clean	2.18	5.80	0.04	9046	20	8.54	50	<mdl	0.09	242	<mdl	0.47	0.81
Porous	2.23	6.21	0.04	2950	11	148	2.07	<mdl	2.58	697	2.34	32	31
Porous aggregate	2.33	8.06	0.06	33286	209	333	4.53	0.36	15	348	7.03	80	32
Porous aggregate	2.62	6.06	0.04	24270	236	353	5.85	0.25	18	348	6.46	19	26
Aggregate, Rim	2.70	8.71	0.04	32319	300	403	5.77	0.50	19	678	6.49	286	75
Large aggregate, Core	2.91	10.73	0.04	16045	103	88	9.53	<mdl	4.53	27	<mdl	0.05	<mdl
Porous	7.62	5.85	0.05	33145	187	298	7.78	0.68	14	373	3.57	267	71
<i>MP54 -3430</i>													
Feathery, Vein	3.46	6.24	0.04	5913	35	11	24	6.17	0.31	82	6.94	117	50
Grain boundary, Alt.	4.82	5.43	0.03	3704	62	80	63	<mdl	1.04	2111	8.83	3407	1760
Feathery, Vein	6.14	5.84	0.04	6139	23	47	71	<mdl	3.79	365	2.88	470	190
Clean, Vein	8.93	5.67	0.04	10513	13	11	36	0.27	0.38	48	0.64	66	33
Clean, Alteration	9.19	5.59	0.03	8079	67	38	50	0.65	1.65	125	3.13	139	61
Feathery, Vein	22	5.32	0.04	8824	388	1586	130	318	41	156	1.17	<mdl	<mdl
Feathery, Vein	22	6.23	0.03	7022	175	418	142	75	17	63	<mdl	<mdl	<mdl
Feathery, Vein	33	5.62	0.04	7845	714	1539	197	479	47	203	6.34	<mdl	<mdl
Feathery, Vein	34	6.33	0.30	6520	639	946	177	330	48	205	3.63	<mdl	<mdl
Feathery, Vein	43	5.13	0.03	5831	677	907	112	972	40	233	2.92	<mdl	<mdl
Feathery, Vein	46	5.91	0.06	5646	239	375	136	35	18	115	0.72	<mdl	<mdl
Clean, Alteration	53	6.90	0.04	7331	225	353	112	89	17	92	3.79	<mdl	<mdl
Feathery, Vein	56	6.35	0.04	6828	303	829	99	255	27	144	0.66	<mdl	<mdl
Feathery, Vein	62	6.53	0.05	7279	525	792	146	275	24	180	4.82	<mdl	<mdl
Feathery, Vein	79	5.64	0.06	8564	252	388	158	53	31	109	0.42	<mdl	<mdl
Feathery, Vein	131	6.24	1.27	11113	315	397	59	991	20	525	51	0.04	<mdl

Sample/Texture	Au (ppm)	Au precision (ppm)	Au mdl (ppm)	As (ppm)	Ag (ppm)	Sb (ppm)	Se (ppm)	Mo (ppm)	Tl (ppm)	Cu (ppm)	Zn (ppm)	Co (ppm)	Ni (ppm)
<i>MP33 - 3542</i>													
Idiomorphic, Siciliclastics	0.35	11.54	0.05	2950	78	1355	2.59	0.11	3.57	190	2.80	93	112
Idiomorphic, Siciliclastics	3.21	9.19	0.05	14794	23	450	23	<mdl	43	697	7.44	54	16
Idiomorphic, Siciliclastics	6.76	9.74	0.06	8824	93	233	43	1.36	14	717	499	0.79	2.74
Idiomorphic, Siciliclastics	13	9.77	0.05	8071	81	595	28	0.42	31	303	3.27	13	15
Idiomorphic, Siciliclastics	15	8.63	0.05	12156	80	660	24	<mdl	22	917	2.32	274	232
Idiomorphic, Siciliclastics	31	8.12	0.05	16421	81	491	17	1.53	37	317	3.97	13	18
Idiomorphic, Vein	182	7.29	0.04	18389	61	78	72	2.62	0.56	890	133	12	30
Idiomorphic, Vein	219	9.37	0.05	16117	130	145	73	1.65	0.92	1056	181	3.41	8.63
<i>MP32 - 3542</i>													
Dirty, Vein	19	7.05	0.15	5466	531	1269	61	2472	85	240	1.86	0.04	<mdl
Dirty, Vein	26	6.67	0.05	6189	574	958	72	4092	86	277	4.48	0.19	<mdl
Dirty, Vein	36	7.56	0.06	8807	810	1481	76	4578	116	391	7.66	0.37	0.28
Dirty, Vein	38	6.54	0.22	7733	692	589	80	5517	90	324	6.84	0.18	<mdl
Dirty, Vein	39	6.40	1.32	7991	713	547	81	3348	72	310	3.11	0.07	0.79
Dirty, Vein	42	7.45	0.23	8765	678	935	83	4813	97	332	8.05	0.20	<mdl
Dirty, Vein	51	6.29	2.89	10161	535	548	83	2395	51	342	1.23	<mdl	0.42
<i>MP41 -3542</i>													
Idiomorphic, Fracture	0.98	8.24	0.03	14112	3.98	21	6.83	<mdl	0.68	94	4.34	99	42
Idiomorphic, Porous, Rim	1.01	7.36	0.02	10478	28	57	14	0.26	5.12	572	6.48	98	40
Idiomorphic, Porous	1.09	7.10	0.03	10794	15	8.03	7.53	0.16	0.43	762	0.92	54	36
Idiomorphic, Porous, Core	1.30	7.64	0.04	4652	20	12	25	<mdl	0.23	1112	0.91	82	18
Large Idio., Porous, Core	1.32	7.17	0.03	6936	135	440	5.58	<mdl	20	1827	8.12	2038	658
Large Idio., Porous, Rim	1.47	7.06	0.04	1950	24	25	37	<mdl	0.81	777	3.36	41	17
Aggregate, Porous	1.78	8.61	0.04	1984	15	260	2.75	<mdl	16	358	18	107	61
Aggregate, Core	1.89	24.12	0.04	11263	2.00	1058	3.34	<mdl	64	172	11	74	62
Idiomorphic, Porous	3.45	6.80	0.03	2114	54	38	28	<mdl	1.75	1989	0.73	34	31
Aggregate, Grain bound.	3.74	11.74	0.04	3461	33	981	23	<mdl	40	397	12	103	49
Idiomorphic	5.40	7.06	0.03	8201	22	94	11	<mdl	9.05	1156	78	784	72
Aggregate, Grain bound.	9.97	6.50	0.04	5678	20	822	9.85	<mdl	44	506	7.71	179	58
Idiomorphic, Porous	12	6.95	0.05	8410	65	114	23	20	10	775	12	398	113

Sample/Texture	Au (ppm)	Au precision (ppm)	Au mdl (ppm)	As (ppm)	Ag (ppm)	Sb (ppm)	Se (ppm)	Mo (ppm)	Tl (ppm)	Cu (ppm)	Zn (ppm)	Co (ppm)	Ni (ppm)
<i>MP49 -3430</i>													
Idiomorphic, Core	28	8.14	0.20	8545	149	43	616	27	3.56	113	0.79	<mdl	<mdl
Large, Idiomorphic	31	6.80	0.04	11568	51	46	376	48	1.23	67	0.62	<mdl	<mdl
Feathery aggregate	37	5.70	0.05	5439	666	877	142	2602	64	327	14	0.37	0.25
Idiomorphic	72	7.62	0.04	17345	62	48	183	143	3.54	109	<mdl	<mdl	<mdl
Idiomorphic	76	6.14	0.04	15567	87	42	169	17	0.74	242	48	<mdl	<mdl
Wispy	79	6.07	0.07	9927	320	464	97	876	35	239	39	0.54	0.48
Aggregate	80	6.45	0.04	14493	165	244	125	158	15	145	3.42	0.09	<mdl
Idiomorphic	80	6.44	0.04	20531	88	52	234	111	4.82	118	<mdl	<mdl	<mdl
Idiomorphic, Rim	81	6.39	0.04	17756	148	73	404	273	8.57	145	1.29	<mdl	0.14
Idiomorphic, Porous	87	6.91	0.05	24597	65	47	98	27	0.76	120	1.04	0.07	14
Idiomorphic	90	8.18	0.04	17642	48	45	157	29	1.18	80	0.82	<mdl	<mdl
Idiomorphic	91	6.12	0.06	21738	105	107	201	529	14	111	3.55	0.15	1.92
Wispy	96	6.59	0.05	13840	102	71	181	4.23	0.68	522	196	<mdl	<mdl
Aggregate	96	5.38	0.04	22636	62	77	59	2.23	1.53	500	1031	<mdl	<mdl
Large, Idiomorphic	99	6.04	0.04	20079	70	59	202	109	4.98	110	1.07	<mdl	<mdl
Large Idiomorphic	114	8.16	0.04	16472	92	75	176	11	2.38	365	17	<mdl	0.14
Wispy	116	20.81	1.17	7898	429	663	86	1432	56	202	7.83	0.19	<mdl
Idiomorphic, Rim	133	5.74	0.70	15211	95	49	85	2.07	0.50	683	260	<mdl	0.34
Aggregate	164	7.85	0.04	31155	571	1251	83	678	131	151	4.91	0.26	0.37
Large, Idiomorphic	287	7.73	0.05	35816	81	46	113	189	6.11	922	95	0.04	<mdl
<i>MP10 -3559A</i>													
Brecciated grain, fractures	0.28	10.47	0.04	13039	21	397	4.45	<mdl	46	565	3.17	49	21
Brecciated grain, fractures	0.59	10.88	0.06	15437	29	55	<mdl	0.17	3.55	513	3.16	306	20
Brecciated grain, fractures	3.39	8.33	0.03	23658	8.82	140	9.16	0.19	16	161	1.12	96	24
Large brecciated, Rim	9.59	13.14	0.03	5867	52	48	100	0.20	1.83	1450	27	179	24
Brecciated grain, Clear	14	7.33	0.03	9822	5.81	148	47	<mdl	13	62	0.95	67	9.97
Brecciated grain, fractures	26	14.36	0.05	11431	72	297	112	0.16	8.31	1221	7.09	287	19
Large brecciated, Clear	47	7.27	0.03	28863	54	239	29	2.95	7.68	175	1.13	44	6.92
Large brecciated, Clear	64	6.57	0.02	24252	29	112	15	<mdl	8.33	36	1.00	15	1.23
Grain boundary	79	6.40	0.03	20815	118	197	36	0.17	34	371	2.38	117	27
Elongate fragment	86	6.38	0.03	11031	20	104	93	<mdl	16	143	2.82	105	30
Large brecciated, Clear	89	6.40	0.04	24983	32	90	36	0.06	4.99	19	0.75	0.86	0.13
Elongate fragment, Fracture	93	6.48	0.03	13339	19	62	109	0.06	12	142	2.05	90	21